ELSEVIER

Chemical Geology 236 (2007) 92 – 111

CHEMICAL GEOLOGY
INCLUDING
ISOTOPE GEOSCIENCE

www.elsevier.com/locate/chemgeo

Radiation damage and alteration of zircon from a 3.3 Ga porphyritic granite from the Jack Hills, Western Australia

Satoshi Utsunomiya [a,*], John W. Valley [b], Aaron J. Cavosie [b,1], Simon A. Wilde [c], Rodney C. Ewing [a]

[a] *Department of Geological Sciences, University of Michigan, Ann Arbor, Michigan 48109-1005, USA*
[b] *Department of Geology and Geophysics, University of Wisconsin, Madison, Wisconsin 53706, USA*
[c] *Department of Applied Geology, Curtin University of Technology, GPO Box U1987, Perth, Australia*

Received 3 November 2005; received in revised form 18 August 2006; accepted 18 September 2006

Editor: C. Gopel

Abstract

Complexly zoned zircons (19 grains, ~3.3 Ga) from a porphyritic granite in the Jack Hills, Western Australia, have been investigated using electron microprobe analysis (EMPA) and transmission electron microscopy (TEM) in order to examine the effects of radiation as a function of dose, as well as the nano-scale microstructure and composition of impurities and secondary alteration phases. In back-scattered electron (BSE) images, zones with bright contrast consist of an almost unaltered zircon with limited amounts of impurity elements. In contrast, the dark zones contain higher concentrations of trace elements: U, Th, Pb, Fe, Y, Ce, Ca and Al. The cumulative doses due to alpha-decay in the dark zones are calculated to be $0.21–1.0 \times 10^{17}$ (alpha-decay events/mg), equivalent to 1.0–4.7 dpa (displacements per atom). These doses are much higher than the dose required for radiation-induced amorphization, as determined by ion-beam irradiation of synthetic zircon, 0.3–1.0 dpa (0–600 °C). However, based on high-resolution TEM observations, none of the zircons are fully amorphous, to the result of annealing under ambient conditions. The concentrations of Ca and Al, which was considered to indicate alteration, increase dramatically at a cumulative dose of 1.6×10^{16} (alpha-decay events/mg). This is the dose at which the first percolation point occurs, as amorphous domains overlap and form an interconnected network. In the altered zones, nanocrystallites of zircon are present with a random orientation, and the amorphous matrix contains the impurity elements. Although the Ce-concentration is extremely high, 1–2 wt.%, the Ce anomaly, Ce/Ce*, does not vary significantly as a function of dose or degree of alteration, indicating that the LREE patterns were overprinted by the fluids with a similar Ce-anomaly. The valence of Ce analyzed by EELS (electron energy loss spectroscopy) is tetravalent in the altered zone, suggesting that the altering fluids were oxidizing.

Keywords: Radiation damage; Zircon; Jack Hills; Alteration; TEM; EELS

---

1. Introduction

Because of zircon's chemical durability and trace concentrations of U and Th, it is the mineral most commonly used in geological dating (Davis et al., 2003). More recently, zircon has also been used in oxygen

---

[*] Corresponding author. Tel.: +1 734 647 5704; fax: +1 734 647 5706.
E-mail addresses: utu@umich.edu (S. Utsunomiya), rodewing@umich.edu (R.C. Ewing).

[1] Current address. Department of Geology, University of Puerto Rico, Mayaguez, 00681-9017 Puerto Rico.

0009-2541/$ - see front matter © 2006 Elsevier B.V. All rights reserved.
doi:10.1016/j.chemgeo.2006.09.003

isotope studies (Valley et al., 1994; Valley, 2003) and, remarkably, this has revealed that the oxygen isotopic systematics of the Early Archean are retained in some zircons, and these results suggest the presence of water at the Earth's surface during the first 400–500 Ma of the Earth's history (Wilde et al., 2001; Mojzsis et al., 2001; Peck et al., 2001; Valley et al., 2002; Cavosie et al., 2004, 2005). The most recent study by Watson and Harrison (2005) has also reported evidence of sediment recycling as early as 4.35 Ga, based zircon–Ti geothermometry. In addition to the geochronological and isotope geology applications, zircon has also been proposed as an important phase for the immobilization of actinides, including Pu from dismantled nuclear weapons (Ewing et al., 1995; Weber et al., 1997, 1998; Ewing, 1999; Ewing et al., 2003). In fact, Pu-doped zircon has been synthesized with 10 wt.% ^{238}Pu (Weber, 1991; Weber et al., 1994). Amorphization generally decreases the chemical durability of zircon; the dissolution rate of amorphous zircon is approximately two orders of magnitude greater than that of crystalline zircon (Ewing et al., 1982; Weber, 2002). Such a difference in the dissolution rate is critically important to the long-term stability of nuclear waste forms used for the immobilization of actinides (Ewing et al., 1988; Ewing, 2005). From the geochronological point of view, the amorphous domains mainly affect the diffusion and leaching rates of multi-isotope elements and can result in discordant ages. In fact, the diffusion coefficient of Pb in radiation-damaged zircon was determined to be 4–5 orders of magnitude greater than that of undamaged zircon; that is, diffusion is facilitated by radiation-induced amorphization (Cherniak et al., 1991; Cherniak and Watson, 2000). A recent study has also shown that Pb selectively concentrates in the amorphous areas created by fission tracks in zircon (Utsunomiya et al., 2004). As a result of each alpha-decay event, several thousand atoms may be displaced, mainly by the ballistic interactions of the alpha-recoil nucleus, creating a damage cascade 2 to 4 nm in diameter (Ewing et al., 2000). The damage process by which the number of cascades increases and finally overlap has been described by percolation theory (Salje et al., 1999; Ríos et al., 2000).

Radiation-induced metamictization has been considered as a potential cause of Pb-loss in geochronological applications (Craig, 1968). However, relaxation and annealing can contribute to structural recovery during the damage accumulation process in natural zircon, and there is strong evidence that annealing occurs under ambient conditions over geologic periods (Nasdala et al., 2001; Palenik et al., 2003; Nasdala et al., 2004). In addition, zircon is susceptible, not only to radiation damage, but also to intense hydrothermal and/or low-temperature alteration (Krogh, 1973; Krogh and Davis, 1975; Balan et al., 2001; Geisler et al., 2003a; Breeding et al., 2004). Several studies have demonstrated that under hydrothermal conditions, Pb-loss from zircon depends on the radiation damage level, temperature, duration of the hydrothermal condition, and solution composition (Sinha et al., 1992; Pidgeon et al., 1966; Rizvanova et al., 2000; Geisler et al., 2001, 2002, 2003b). Previous studies of zircon reported that heavily radiation damaged portions commonly contain more than a few wt.% of impurities, such as Ca and Al, introduced as a result of alteration (Krogh and Davis, 1975; Geisler et al., 2003a).

Zircons from Jack Hills and the surrounding Narryer Terrane have been studied extensively since the 1980s in order to find evidence of continental crust on the Earth before 4.0 Ga, based on analyses on detrital zircons from meta-sedimentary rocks (Froude et al., 1983; Compston et al., 1985; Compston and Pidgeon, 1986; Maas and McCulloch, 1991; Maas et al., 1992). The geological setting and the geochronology of Jack Hills and the surrounding Narryer gneiss complex, have been described in detail by Myers and Williams (1985), Myers (1988), Nutman et al. (1991), Pidgeon and Wilde (1998) and Nelson et al. (2000). The zircon samples in this study (#W61 of Pidgeon and Wilde, 1998) were collected from an outcrop of porphyritic granitoid, approximately 3 km south of the meta-conglomerate site in the Jack Hills where the most ancient zircons were collected (Compston and Pidgeon, 1986; Wilde et al., 2001; Mojzsis et al., 2001). The unzoned cores of W61 zircons give a concordant age; whereas, the zoned portions were discordant (Pidgeon and Wilde, 1998). The crystallization age was determined to be 3290±20 (2σ) Ma. In addition, an isotopic disturbance, such as alteration in the presence of a fluid may have occurred at ~200 Ma, based on the lower intersection ages on the concordia plot (Pidgeon and Wilde, 1998).

Because of the great age (3.3 Ga) of these zircon samples and their geologic significance, we have completed a detailed, nano-scale investigation of their structure and composition. This is important because ion probe analyses of zircon are generally conducted on micron-sized areas; however, the possibility of nano-scale heterogeneity is important to the proper interpretation of these data. Up until now, there has been little effort to characterize the nano-scale features of the zircons from the Jack Hills granitoids of western Australia. The essential questions include: (i) What is the occurrence of the nano-scale inclusions?, (ii) What is the nano-structure of the damage domains after 3.3 Ga.?, (iii) What has been the effect of the multiple alteration events on the nano-scale structure and composition of these zircons?, (iv) What is the relation between the damaged nano-structure and compositional variations caused by thermal annealing and hydrothermal alteration? In order to overcome the spatial resolution problem, we have utilized a variety of electron microscopy techniques, obtaining information on the compositional variation, of the nano-structure, inclusions, and the oxidation state of the multi-valent cations in the zircons.

2. Experimental method

Back-scattered electron imaging was completed using scanning electron microscopy, SEM (HITACHI S3200) with an accelerating voltage of 15 kV. Point chemical analyses were conducted by electron microprobe analysis, EMPA (Cameca, SX-100). EMPA was operated using a focused electron-beam (a few μm in diameter) with an accelerating voltage of 20 kV and probe current of 100 nA. Counting time was 60 s for all elements, except that Zr and Si, which were measured for 30 s. The standard specimens used for calibration were: andradite for Ca (K_α), Si (K_α) and Fe (K_α), zircon for Zr (L_α), albite for Al (K_α), REE glass standards (Drake and Weill, 1972) for La (L_α), Ce (L_α), Nd (L_α), and Y (L_α), synthetic crystals of UO_2 for U (M_β), HfO_2 for Hf (M_α), PbS for Pb (M_α), and ThO_2 for Th (M_α). The Cameca PAP correction routine (modified ZAF) was used for data reduction. Interferences on the peaks and background positions due to overlap of other elements were avoided during setting the data acquisition condition. The detection limits under these conditions are 25 ppm for Al, 170 ppm for Si, 55 ppm for Ca, 85 ppm for Fe, 155 ppm for Y, 1600 ppm for Zr, 180 ppm for La, 175 ppm for Ce, 165 ppm for Nd, 95 ppm for Hf, 230 ppm for Pb, 205 ppm for Th, and 250 ppm for U.

Nano-scale characterization was done by high-resolution transmission electron microscopy (HRTEM) using a JEOL 2010F. The TEM specimens were prepared by mechanical polishing to a thickness of a few tens of μm, followed by ion milling (GATAN PIPS) using 4.0 kV Ar ions. High-angle annular dark-field scanning transmission electron microscopy (HAADF-STEM) with energy dispersive X-ray spectrometry (EDS) was employed for Z-contrast imaging and nano-scale elemental mapping. The detailed procedure of HAADF-STEM imaging has previously been described in Utsunomiya and Ewing (2003). In general, the contrast in HAADF-STEM is correlated to mass, density, periodicity of atoms and sample thickness (Utsunomiya et al., 2005), and the major advantage is that the contrast does not change significantly near "just focus" due to the incoherent imaging process (Pennycook and Jesson, 1990).

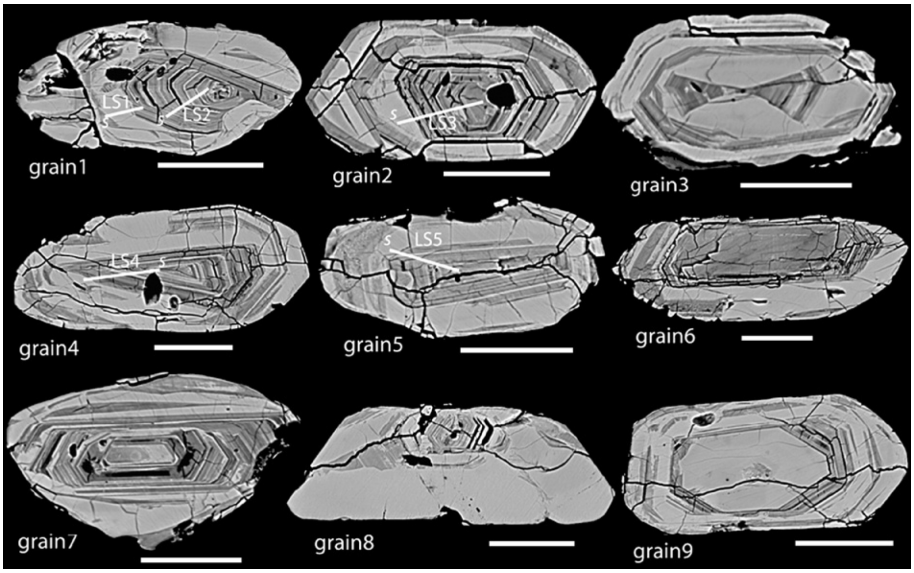

Fig. 1. Back-scattered electron (BSE) images of zircon grains prepared for EMPA from porphyritic granitoid W61 from the Jack Hills, Western Australia. The scale bars are 50 μm. The position of quantitative line scan analyses is indicated by white lines labeled as "LS" with numbers. The starting point of analysis is marked with a symbol "*s*".

The oxidation state of trace amounts of Ce in zircons was qualitatively analyzed by parallel electron energy-loss spectroscopy (PEELS) using a Gatan Imaging Filter system. The oxidation state of Ce can be determined by detailed examination of ELNES (energy-loss near-edge shape) of the Ce M-edge (Garvie and Buseck, 1999). The JEOL2010F at the University of Michigan has a FWHM (full-width-at-half-maxima) of the zero-loss peak in EELS profile as ~1.0 eV for a 4.0 s acquisition. This energy resolution becomes greater than 1.0 eV for a longer acquisition time, which is the case for trace elements due to the low signal/background ratio. Because the energy resolution was not high enough to do quantitative analysis, the valence state analysis using EELS was performed qualitatively. The entrance aperture of EELS was 0.6 mm, and an energy dispersion of 0.1 eV/channel was used. Only thin areas in the specimen were analyzed to minimize the effect of the multiple inelastic scattering on the fine structure of core-loss edges.

In the present study, zoning in nine zircons was analyzed by EMPA. Four additional grains were also analyzed for an incomplete set of elements (IC-series). Each grain was analyzed at 30–45 sites. Six other grains were used for the TEM observations (labeled as T). TEM specimens were observed by SEM before and after ion milling to check the exact position of the TEM observation.

3. Results

3.1. Chemical zonation

BSE images of zircons from the porphyritic granite (Fig. 1) revealed extensively developed zoning, ~1 μm to ~10 μm in width, with some oscillatory zoning

Table 1
Representative composition (in oxides wt.%) in bright and dark zones in BSE images of zircon from Jack Hills granitoid sample W61

	ZrO_2	SiO_2	HfO_2	Al_2O_3	P_2O_5	CaO	FeO[a]	Y_2O_3	La_2O_3	Ce_2O_3	Nd_2O_3	PbO	ThO_2	UO_2	Total
Bright zone in BSE image															
Grain 1	65.66	32.68	2.008	UDL[b]	UDL[b]	UDL[b]	0.033	0.044	UDL[b]	UDL[b]	UDL[b]	0.049	UDL[b]	0.060	100.57
	(1.18)	(0.56)	(0.096)				(0.023)	(0.018)				(0.022)		(0.025)	
Grain 2	63.39	29.55	1.734	0.975	1.843	0.235	0.735	0.199	0.089	0.370	0.140	0.086	0.061	0.239	99.64
	(1.18)	(0.56)	(0.088)	(0.015)	(0.023)	(0.009)	(0.033)	(0.018)	(0.020)	(0.023)	(0.020)	(0.023)	(0.019)	(0.026)	
Grain 3	66.58	31.92	1.326	UDL[b]	0.064	0.010	0.029	0.160	UDL[b]	0.019	UDL[b]	0.032	0.041	0.050	100.25
	(1.24)	(0.61)	(0.067)		(0.010)	(0.007)	(0.008)	(0.017)		(0.017)		(0.022)	(0.019)	(0.024)	
Grain 4	66.09	32.52	1.746	0.013	UDL[b]	0.039	0.019	0.021	UDL[b]	0.039	UDL[b]	UDL[b]	UDL[b]	0.049	100.55
	(0.62)	(0.29)	(0.020)	(0.002)		(0.007)	(0.007)	(0.014)		(0.016)				(0.024)	
Grain 5	66.91	32.64	1.650	0.004	UDL[b]	0.017	0.032	0.051	UDL[b]	0.031	UDL[b]	0.036	UDL[b]	0.058	101.44
	(0.62)	(0.29)	(0.020)	(0.002)		(0.007)	(0.008)	(0.014)		(0.017)		(0.022)		(0.024)	
Grain 7	64.92	32.00	1.596	0.194	0.134	0.071	0.292	0.128	UDL[b]	0.277	0.095	0.026	0.022	0.115	99.88
	(0.61)	(0.28)	(0.019)	(0.003)	(0.010)	(0.007)	(0.011)	(0.016)		(0.019)	(0.016)	(0.021)	(0.018)	(0.024)	
Grain 8	66.51	32.60	1.587	UDL[b]	0.059	UDL[b]	0.023	0.166	UDL[b]	UDL[b]	UDL[b]	0.051	0.021	0.060	101.09
	(1.24)	(0.62)	(0.080)		(0.010)		(0.008)	(0.017)				(0.022)	(0.018)	(0.024)	
Dark zone in BSE image															
Grain 1	57.77	26.88	1.732	1.624	3.771	0.576	1.514	0.719	0.117	1.228	0.609	0.062	0.215	0.495	97.32
	(1.08)	(0.515)	(0.087)	(0.025)	(0.034)	(0.013)	(0.064)	(0.026)	(0.019)	(0.031)	(0.024)	(0.022)	(0.020)	(0.027)	
Grain 2	53.49	23.76	1.627	3.581	4.859	0.527	2.107	0.305	0.180	0.943	0.371	0.044	0.133	0.461	92.39
	(1.01)	(0.457)	(0.082)	(0.054)	(0.040)	(0.012)	(0.088)	(0.019)	(0.021)	(0.029)	(0.022)	(0.021)	(0.019)	(0.027)	
Grain 3	59.59	31.41	1.261	0.559	0.375	0.178	2.673	0.306	0.049	0.581	0.210	0.060	0.270	0.233	97.75
	(1.12)	(0.601)	(0.064)	(0.009)	(0.012)	(0.008)	(0.111)	(0.020)	(0.017)	(0.024)	(0.019)	(0.022)	(0.021)	(0.025)	
Grain 4	58.09	28.27	1.436	1.242	3.658	0.478	1.367	0.303	0.114	0.803	0.417	0.052	1.210	0.530	97.96
	(0.56)	(0.25)	(0.018)	(0.009)	(0.029)	(0.011)	(0.034)	(0.019)	(0.019)	(0.028)	(0.021)	(0.021)	(0.033)	(0.028)	
Grain 5	59.45	28.75	1.547	1.016	1.224	0.389	1.177	0.348	0.090	1.768	0.326	0.081	0.1480	0.394	96.71
	(0.57)	(0.26)	(0.019)	(0.007)	(0.018)	(0.010)	(0.030)	(0.021)	(0.019)	(0.041)	(0.020)	(0.023)	(0.020)	(0.027)	
Grain 7	46.71	29.93	0.912	1.189	1.561	0.440	5.493	0.589	0.142	1.452	0.767	0.024	0.471	0.837	90.52
	(0.48)	(0.27)	(0.015)	(0.008)	(0.020)	(0.010)	(0.125)	(0.024)	(0.019)	(0.036)	(0.024)	(0.021)	(0.023)	(0.031)	
Grain 8	53.71	28.26	1.519	0.568	0.448	0.193	3.869	0.567	0.125	0.709	0.413	0.020	2.854	0.346	93.60
	(1.01)	(0.54)	(0.077)	(0.009)	(0.013)	(0.008)	(0.160)	(0.024)	(0.020)	(0.026)	(0.022)	(0.024)	(0.044)	(0.027)	

The values in parenthesis are the standard deviation.

[a] All Fe as FeO.

[b] UDL means the analyzed values were under the detection limit.

replaced by unzoned domains. These unzoned portions, intersecting the zoned areas, were obviously formed after the formation of oscillatory zoning, which Pidgeon and Wilde (1998) dated as 3290 Ma. The contrast of zoning in BSE images reflects the variation in the average mass of the elements in these zones. Hereafter "bright zone" and "dark zone" correspond to the contrast in BSE image. Representative compositions determined by EMPA for the bright and the dark zones are given in Table 1. The darker zones contain trace amounts of Al, Ca, Fe, REEs, Pb, Th and U, and are depleted in Zr, Si and Hf. Analyses of the dark zones do not sum to 100 wt.% and are low by ~10 wt.%. Such low totals are common for altered zircon (Krogh and Davis, 1975) and are generally ascribed to the presence of H_2O introduced during secondary alterations (Geisler et al., 2003a). The substitution of water in radiation-damaged zircon has also been demonstrated by infrared spectroscopy (Aines and Rossman, 1986; Geisler et al., 2003c).

A SiO_2 vs. ZrO_2 plot (Fig. 2a) reveals that Si decreases as Zr decreases (Fig. 2a), and the alteration trend for each grain is slightly different as alteration

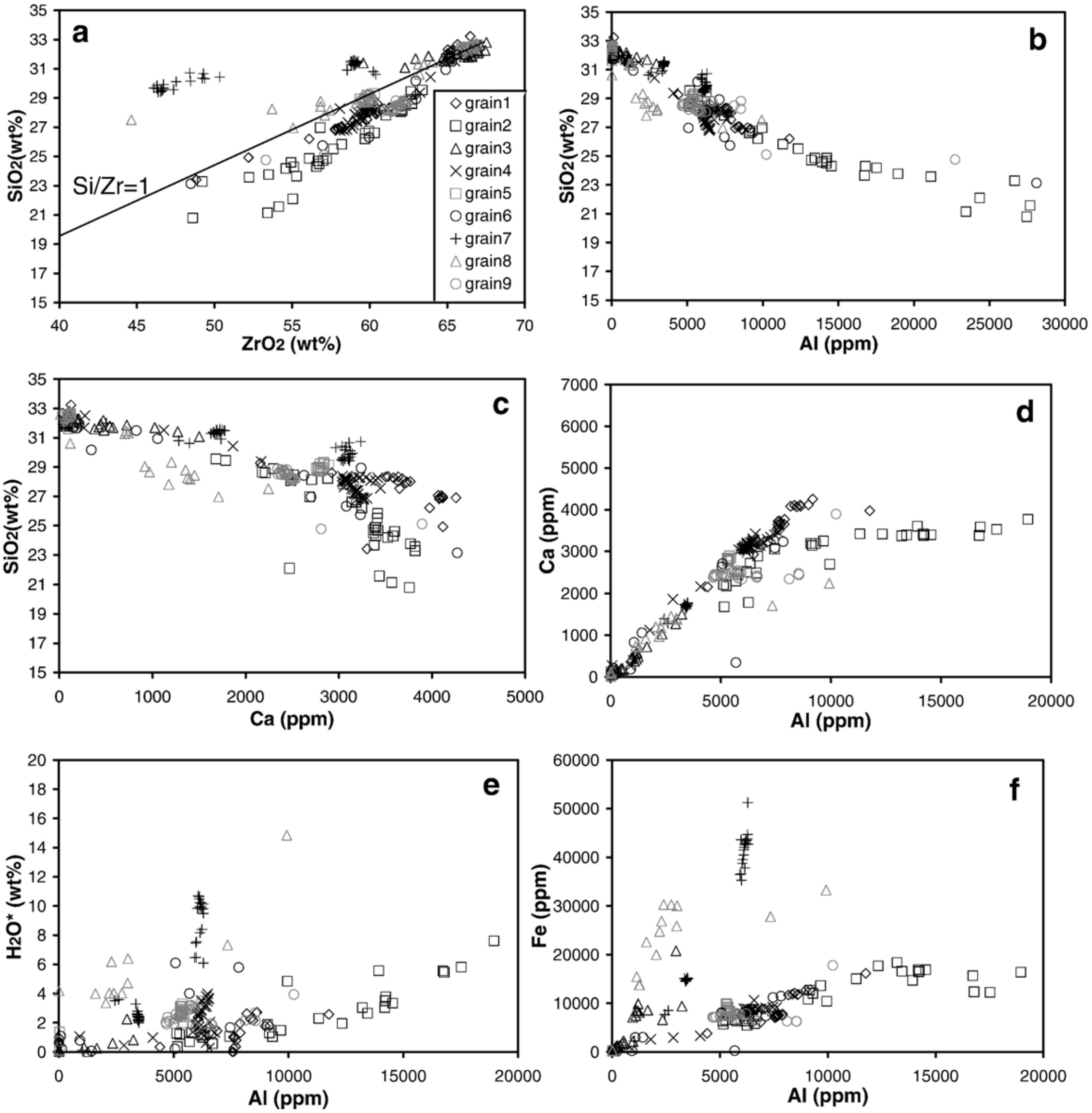

Fig. 2. Plots of EMPA results: (a) SiO_2 (wt.%) vs. ZrO_2 (wt.%). The solid line is for Si:Zr = 1:1 (atomic ratio); (b) SiO_2 (wt.%) vs. Al (ppm); (c) SiO_2 (wt.%) vs. Ca (ppm); (d) The correlation between Ca and Al; (e) H_2O* (which stands for the variation from 100 wt.% in the analytical total) vs. Al (ppm); (f) Fe (ppm) vs. Al (ppm); (g) Y (ppm) vs. Al (ppm); (h) Ce (ppm) vs. Al (ppm); (i) Y (ppm) vs. P (ppm); and (j) Ce (ppm) vs P (ppm).

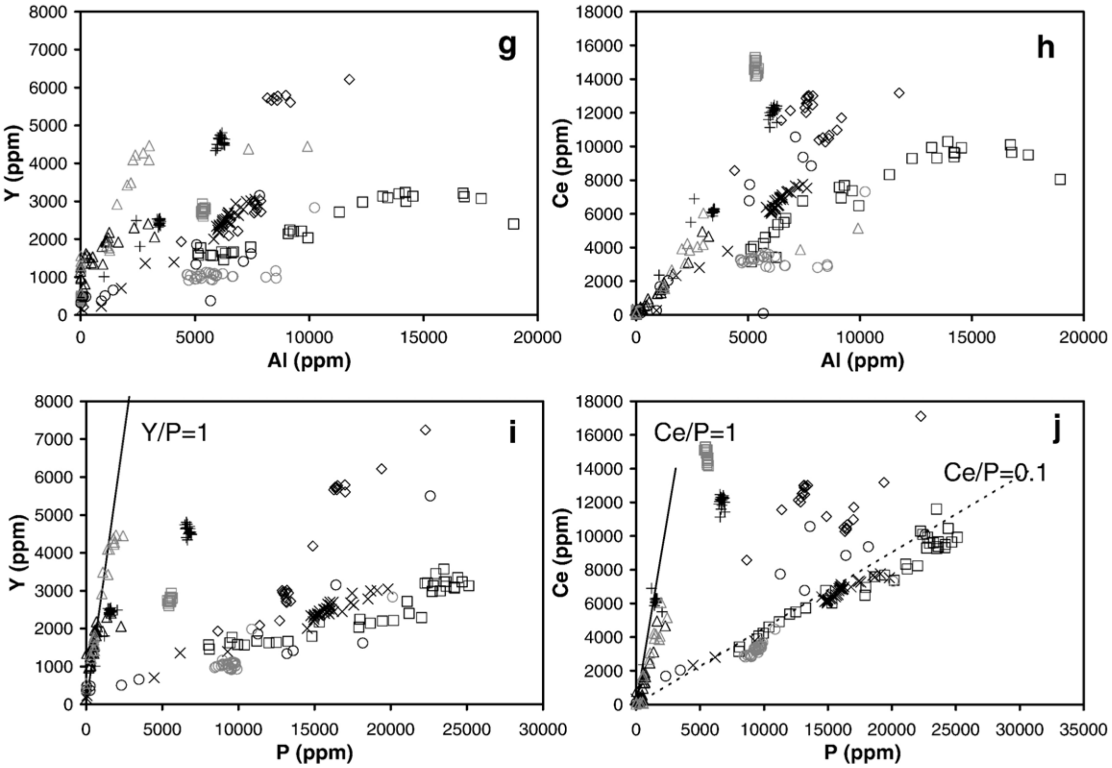

Fig. 2 (*continued*).

proceeds: in some grains (grains 1, 2, 4, 6, and 9) the trend is shifted toward Si/Zr<1 (atomic ratio), and for a few grains (grains 3, 7 and 8) the shift is toward Si/Zr>1 as the alteration proceeds. A hydrothermal experiment on partially metamict zircon has also shown similar trends of SiO_2–ZrO_2 variation as a result of different compositions and temperatures of the altering fluids: trends towards Si-rich (Si/Zr>1), towards Zr-rich (Si/Zr<1), and of dissolution along stoichiometry (Si/Zr=1) (Geisler et al., 2003b).

The SiO_2 vs. Al plot and SiO_2 vs. Ca plot show that SiO_2 decreases linearly as both Al and Ca increase (Fig. 2b and c). Because such high concentrations of Ca and Al cannot be incorporated into the initial zircon, Ca and Al were used as evidence of alteration in a previous study of zircon alteration (Geisler and Schleicher, 2000). Aluminum was used as evidence of alteration in this study based on the close correlation between Ca and Al (Fig. 2d), although the Al content increased more rapidly at high concentrations of Al.

Although the main reason for the low totals by EMPA is most likely because of the presence of water in the altered zones, other factors such as heavy REEs content, which were not analyzed, might also contribute to the lower totals. Thus, the deference between the analysis total and 100% is hereafter labeled as H_2O*. The H_2O* values plotted against Al show a trend of H_2O* increasing as Al increases, indicating that the amount of water is correlated to the extent of alteration (Fig. 2e). Points that are scattered well away from the trend line may be ascribed to the analysis being located at crystal imperfections, such as on cracks.

The Fe, Y and Ce concentrations increase linearly with the increase in Al (Fig. 2f–h), but there is a wide variation in the slope of the data for each grain. For example, the Fe concentration in grains 3, 7 and 8 (Fig. 2f) increases with a much higher Fe/Al ratio than the other grains, as do Y and Ce in the same grains. This suggests that there is a variation in the composition of the altering fluids; Fe/Al and Ce/Al. The Y vs. P plot (Fig. 2i) revealed that all points in grains 3, 8, and for some points in grain 7 fall on a line of Y/P=1, which is consistent with xenotime substitution (Hanchar et al., 2001). However, the P-content of all the other grains are in excess of Y/P=1, probably due to the P-rich altering fluid. The linear correlation between Y and P for these grains indicates that the Y content was also correlated with the P content of the fluid. Phosphorous concentration in the fluids was also correlated with the Ce concentration (Fig. 2j).

Fig. 3 shows the results of quantitative line scan analyses across the zoning in four grains (grains 1, 2, 4 and 5) shown in Fig. 1. The Hf concentration appears to be unrelated to the zoning pattern. On the other hand, all the other trace elements are abundant in the dark zones. The transition between dark and bright zones seems to be gradual because the beam size of EMPA is not small enough to detect sharp changes in concentration. A detailed analysis for the boundary at higher resolution will be shown in the discussion of the TEM results in a later section. Distribution of Fe is different from the other elements, as clearly seen in LS 1 and 5, although the concentration is low in the bright zones, along with most other elements, indicating that the alteration event that precipitated Fe inside zircon grains occurred at a different time from the alteration that delivered the other impurity elements. In a few cases, Th concentration is also unrelated to the other trace elements, as shown by extremely high Th-concentration near the point "*s*" of LS-5 in grain 5, indicating that the alteration fluids were sometimes enriched in Th.

3.2. *Calculated cumulative dose and trace element distribution*

The total cumulative dose, D_α (α-decay events/mg), was calculated based on U and Th concentrations following Ewing et al. (2000);

$$D_\alpha = 8N_1[\exp(\lambda_1 t)-1] + 7N_2[\exp(\lambda_2 t)-1] + 6N_3[\exp(\lambda_3 t)-1] \qquad (1)$$

where N_1, N_2, and N_3 are the present values of ^{238}U, ^{235}U, and ^{232}Th, respectively, in atoms/mg; λ_1, λ_2, and λ_3 are the decay constants for ^{238}U, ^{235}U, and ^{232}Th, respectively, in years^{-1}; and t is the age of the zircon. The cumulative dose in dpa units is calculated based on the equation including results of SRIM (Stopping and Range of Ions in Matter) (Ziegler et al., 1985) calculation;

$$\text{Dose (dpa)} = 9.40 \times 10^5 \times D_\alpha \times M/(N_A \times 6) \qquad (2)$$

where M is the molar mass of zircon and N_A is Avogadro's number.

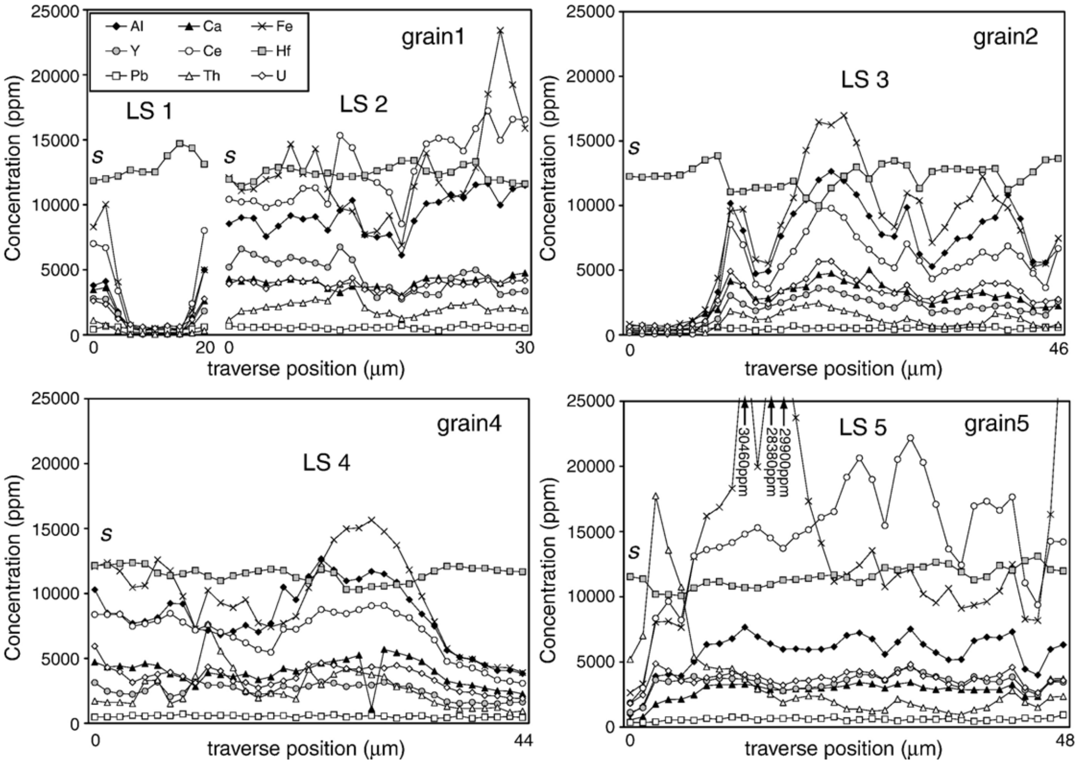

Fig. 3. Quantitative line scan analysis of trace elements (ppm) across the zones of grains 1, 2, 4, and 5 (Fig. 1). The position of analyzed line is indicated in Fig. 1. The starting points "*s*" also corresponds to the point of "*s*" in Fig. 1. The line in grain 1 was split into two lines (LS 1 and 2) to avoid analyzing across a fracture.

Fig. 4a–f shows graphs of H_2O*, Al, Ca, Th and Hf data as a function of the calculated cumulative dose. The Al, H_2O* and Ca plots show an increase as the dose increases. These results indicate that the amorphous domains in the zircon structure created by α-decay events provided pathways by which Al, Ca and H_2O*

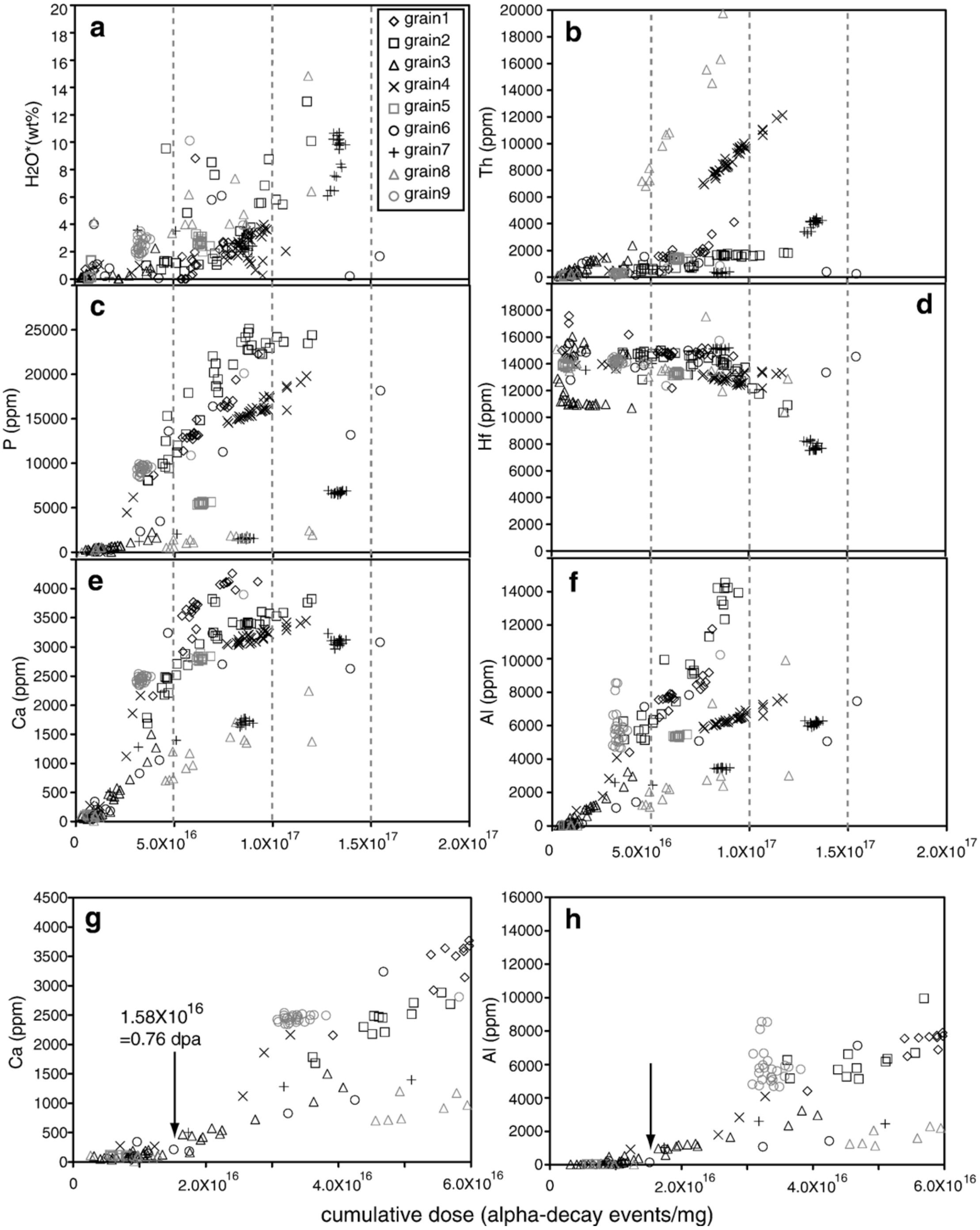

Fig. 4. Trace elements and H_2O^* data plotted versus the calculated cumulative dose: (a) H_2O^* (wt.%); (b) Th (ppm); (c) P (ppm); (d) Hf (ppm); (e) Ca (ppm); and (f) Al (ppm). Calucium and Al plots magnified over the cumulative dose are shown in (g) and (h). The arrows indicate the points where impurities begin to increase.

can easily penetrate the zircon structure. Although the cation data in Fig. 4 plot over a wide range, there is a maximum upper limit to all slopes. This maximum slope represents the volume fraction of crystalline to amorphous domains. Although Th-concentration also reveals a positive linear correlation with the cumulative dose, it is simply because Th is one of the parameters in calculation of the dose. In the Hf plot (Fig. 4d), two groups with different concentrations appear in grains 1, 3 and 9. The variation is not related to zoning or U distribution in zoning. Although there are two separate concentrations at the low doses, the concentrations gradually decrease as the dose accumulates. The decrease of Hf is due to the occurrence of amorphous domains, from which Hf is gradually leached from the grain.

The majority of the calculated doses are within the range $<1.5\times10^{17}$ (alpha-decay events/mg), which is equivalent to <7.3 dpa. Some data points from grains 5, 6 and 8 plot above 4.7 dpa, and the highest dose reached is nearly 2.5×10^{17} (alpha-decay events/mg), which is equivalent to 12 dpa. Even a dpa value of 7.3 is much higher than the critical amorphization dose for zircon, which was previously determined by well-controlled ion irradiation experiments; 0.3 dpa (at room temperature) to 1.0 dpa (~873 K) (Weber et al., 1994; Meldrum et al., 1998a,b). Fig. 4g and h show Ca and Al plots enlarged along the cumulative dose, showing that these impurities start increasing at $\sim1.6\times10^{16}$ (alpha-decay events/mg), which is equivalent to 0.76 dpa.

3.3. TEM results

Fig. 5 shows BSE images of six grains prepared for TEM observation. These grains reveal well-developed oscillatory zoning. Some grains contain several inclusions within the oscillatory zoning which can be resolved by SEM analysis as shown in images T2 and T3.

At the spot A in grain T1, the HAADF-STEM image shows a slight difference in contrast; some areas appear as bright patches generally within a dark area (Fig. 6a). The EDS analyses reveal a slight difference in trace element content, as shown in Y content, between the dark and bright contrast (Fig. 6b and c). The SAED and HRTEM from both areas did not show amorphous domains, but only crystalline zircon. Such a slight difference in composition resulted in the differences in contrast in the HAADF-STEM image. In addition, numerous pores occur at 10–100 nm, associated with the relatively bright contrast areas. Inclusions were also found at the spot B in grain T1 (Fig. 6d). Two adjacent inclusions have different compositions; inclusion 1 contains Mg, K, and Ti; whereas, inclusion 2 has increased amounts of Fe (Fig. 6e and f). In both inclusions, Zr and Si peaks in EDS provide a signal from matrix zircon. Although the diffraction pattern was not possible due to the thickness of this area, the compositions indicate that inclusion 1 consists of a clay mineral such as phengite or illite, and inclusion #2 is a mixture of Fe-oxide with a small amount of alumino-silicates.

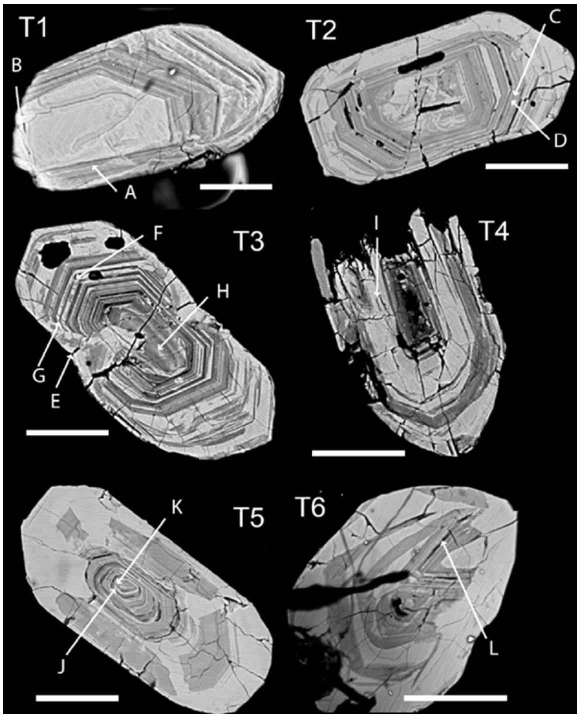

Fig. 5. BSE images of zircons prepared for TEM analysis. These grains were attached to Cu-grids. The positions indicated by letters correspond to the spot of TEM observations. Grain T6 shows dark contamination by resin, but the resin was removed during ion milling and cleaned before TEM observation.

Grain T2 shows well-developed sharp oscillatory zoning, <1 μm. In HAADF-STEM image of the spot C, the image contrast matches the contrast in BSE image because of the variation in the average mass (Fig. 7a). The “bright” and “dark” zones in the following TEM results section correspond to the contrast in HAADF-STEM, but these are almost same as the contrast in BSE image. The bright zone (zone 1) consists of crystalline zircon without impurity elements; whereas, the dark contrast zone (zone 2) shows randomly oriented nano-sized crystallites in an amorphous matrix (Fig. 7b and c). The EDS of zone 2 also reveals the presence of non-formula elements: Al, Th, Ce, (and Fe) are clearly shown in the enlarged profile (Fig. 7e). In addition, a number of pores are also present (Fig. 7f). The pores

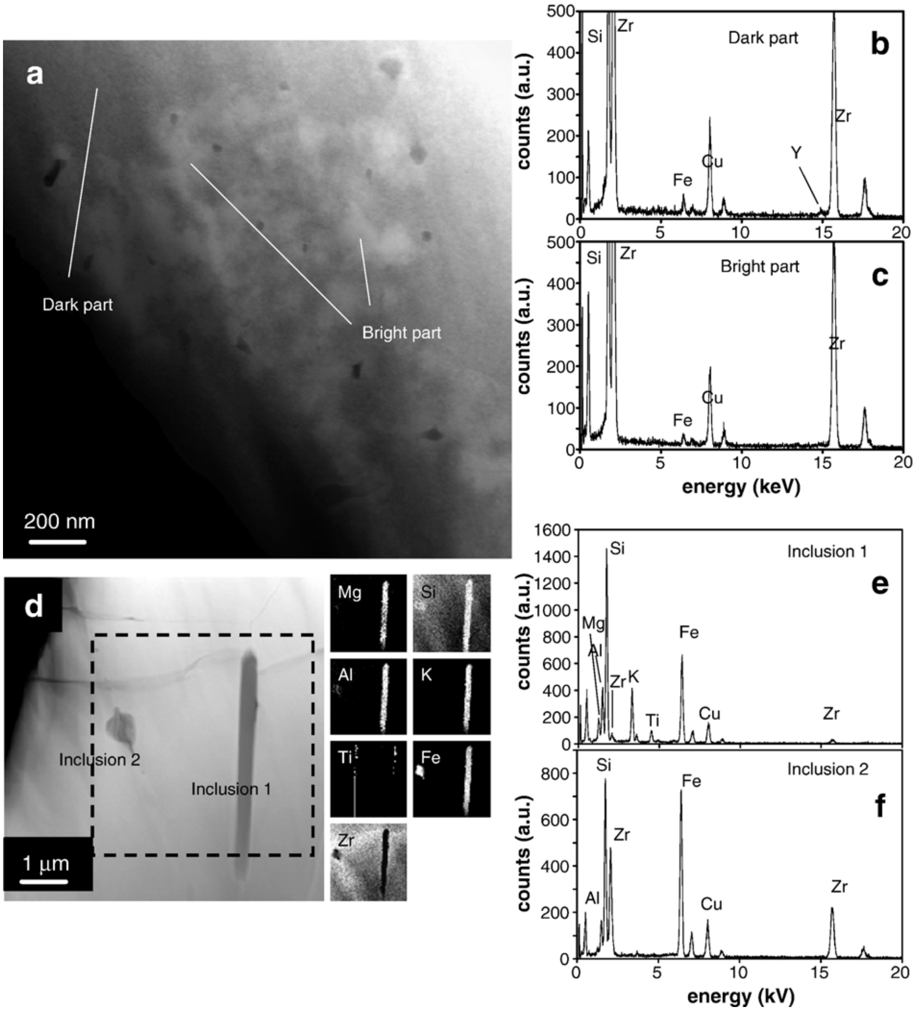

Fig. 6. (a) HAADF-STEM image showing slight differences in contrast at spot A in grain T1. (b) and (c) EDS from dark and bright contrast area, respectively. The Cu-peak is from the Cu-grid. (d) HAADF-STEM image with elemental map of the dotted square region for inclusions at spot B in grain T1. (e) and (f) EDS from the inclusions 1 and 2, respectively. The Cu-peak is from the Cu-grid.

occur in dark contrast and medium gray zones making an array along the zoning; whereas, there is no pore in the bright zones. HRTEM image shows that the edge of the pore is formed by a termination of crystalline zircon (Fig. 7g). A small amount of amorphous material is found inside the pore. Another inclusion at spot D in grain T2 consists of Fe-oxide, which cuts across the zoning (Fig. 7h). This texture indicates that the Fe-inclusion formed when the zircon grain crystallized or another phase was crystallized first and then replaced by Fe-oxides. A result of STEM line scan analysis is shown in Fig. 7i, associated with the corresponding zoning image, which clearly reveals that the dark contrast zone has retained relatively higher non-formula elements than the bright zone, even at the submicron scale. Because the EDS data profile for each analysis point is not processed with background subtraction or other semi-quantification, this profile shows only the relative abundance of trace elements in these zones.

A large volume of secondary alteration phases fill cracks and cleavages at spot E in grain T3, (Fig. 8a). Based on the HRTEM image, SAED showing a layer structure with ~1.0 nm lattice spacing (Fig. 8b), and EDS (Fig. 8c), the secondary phase may be a phengite clay. At spot F, a sequence of zircon structures across the zoning was monitored with SAED (Fig. 8d). The structure in the darker zones retains a certain degree of damage resulting in diffuse diffraction maxima in SAED (zone IV) and randomly oriented zircon nanocrystals are present in zone II, while the bright contrast zones (zone I and III) reveal no diffuse diffraction maxima. Semi-quantitative spot analyses of trace elements were

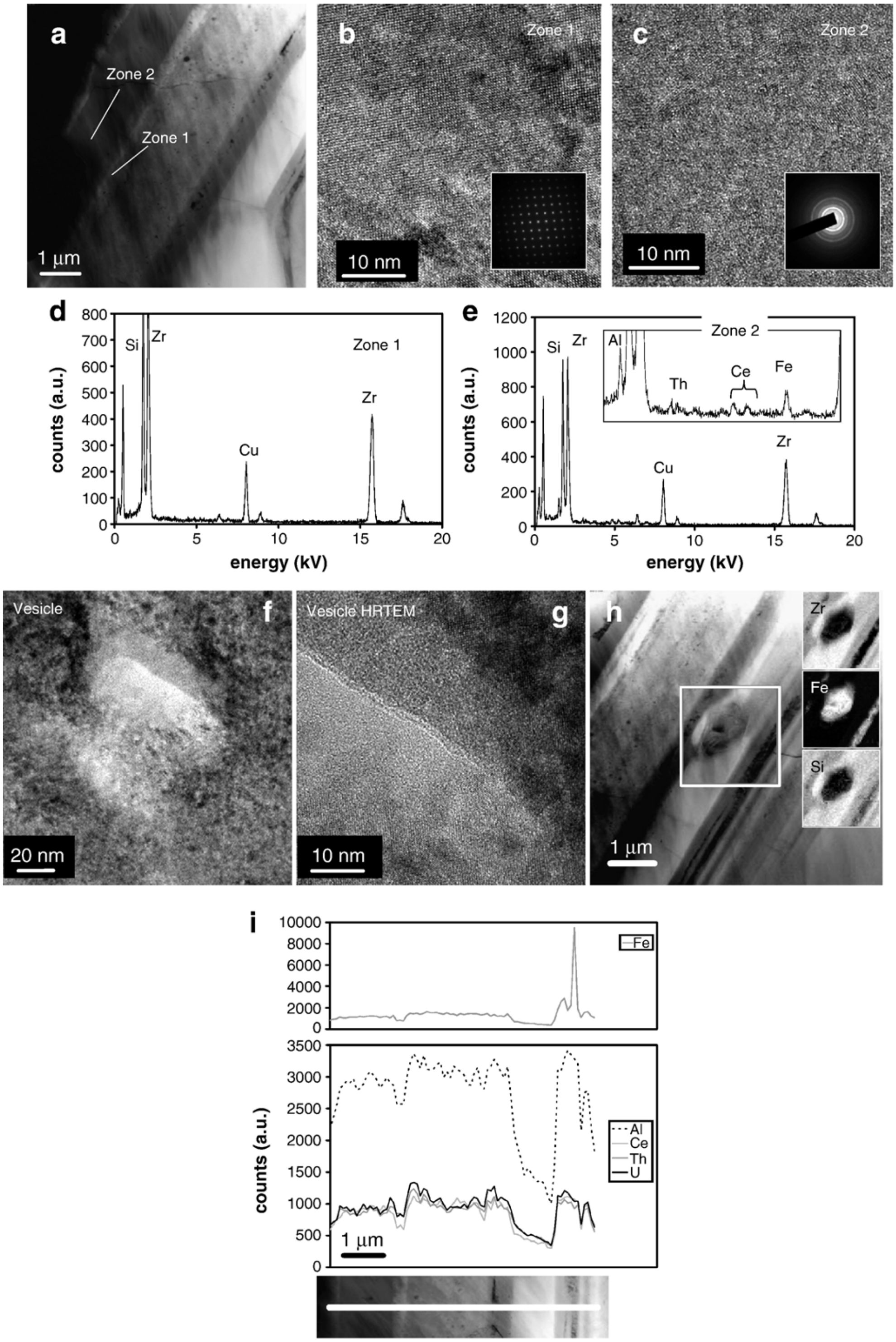

Fig. 7. Spot C in grain T2. (a) HAADF-STEM image showing oscillatory zoning. Bright and dark zones were labeled as zone 1 and zone 2, respectively. (b) and (c) are HRTEM images for zone 1 (bright) and zone 2 dark (dark) with SAED pattern as insets. (d) and (e) are the EDS profile of zone 1 and zone 2, respectively. The Cu-peak is from the Cu-grid. (f) Bright-field (BF) TEM Image of a pore. (g) A magnified HRTEM image of the pore. (h) HAADF-STEM image of an Fe-rich inclusion with elemental maps of the square region located at spot D. (i) EDS line scan profiles obtained in the STEM mode showing the relative variation in the trace elements concentrations across the oscillatory zoning (HAADF-STEM image at the bottom) at area D.

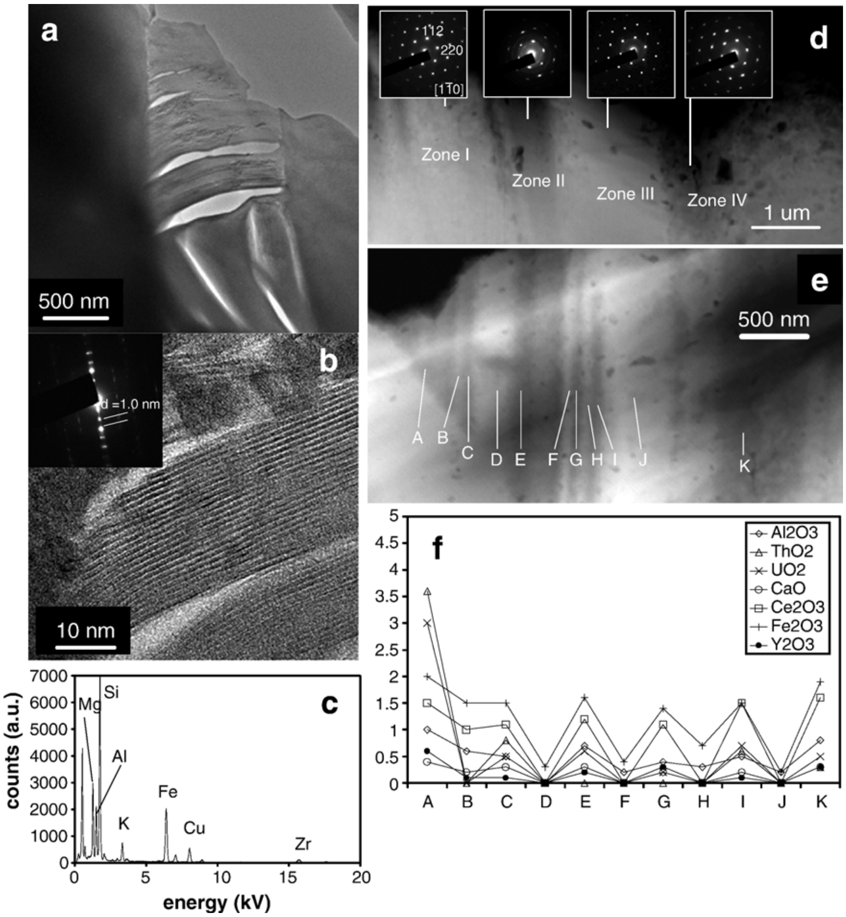

Fig. 8. (a) Secondary alteration phase occurring within a fracture of zircon at spot E in grain T3. (b) The HRTEM images of the alteration phases showing the lattice fringes of ~1.0 nm, as confirmed by SAED pattern (inset). (c) EDS of the secondary phase. The Cu-peak is from the Cu-grid. (d) HAADF-STEM images of zoning at spot F in grain T3 with the corresponding SAED patterns (insets). (e) HAADF-STEM image with alphabetical labels indicating the location of semi-quantitative analyses at spot G in Fig. 5. (f) Compositions of non-formula elements determined by semi-quantitative EDS analysis (wt.%).

conducted through a zoning (Fig. 8e and f). These trace elements appear to be constant at a few wt.% in the dark zones; whereas, the bright zone contains less than 1 wt. %, which is almost below the detection limit of EDS. At spot G, a part of the zoning is overprinted by a bright contrast area (area 1) with irregular dark area (area 2) adjacent to it (Fig. 9a). The SAED from area 1 shows only a zircon diffraction pattern without any diffuse diffraction maxima. The composition of area 1 reveals only zircon constituent elements, while the darker area 2 contains a variety of non-formula elements similar to other dark contrast zones (Fig. 9b and c). However, in contrast to the other dark zones showing ring patterns, area 2 consists of crystalline zircon as evidenced by HRTEM and SAED (Fig. 9d), which may suggest that it formed by recrystallization synchronous with area 1. The evidence that area 1 cuts across the zoning may indicate that recrystallization occurred after alteration of the grain. Fig. 9e from the central core (spot H) of grain T3 shows the preservation of zircon with some magmatic texture. However, the composition of the surrounding dark contrast matrix has some amount of impurity elements, indicating that even the core of the grain was subjected to alteration (Fig. 9f).

In grain T4, alteration products were also present in the form of inclusions at spot I (Fig. 10a).The alteration phase has a layer structure with 1.0 nm lattice fringe (Fig. 10b). Based on the composition by EDS, the phase is also identified as belonging to the phengite series (Fig. 10c). In addition, the alteration phase appeared to occur preferentially oriented with respect to the surrounding zircon; that is, the 1.0 nm repetition is stacked along the [101] direction of the zircon, which may imply epitaxial crystallization. Elsewhere near spot I in grain

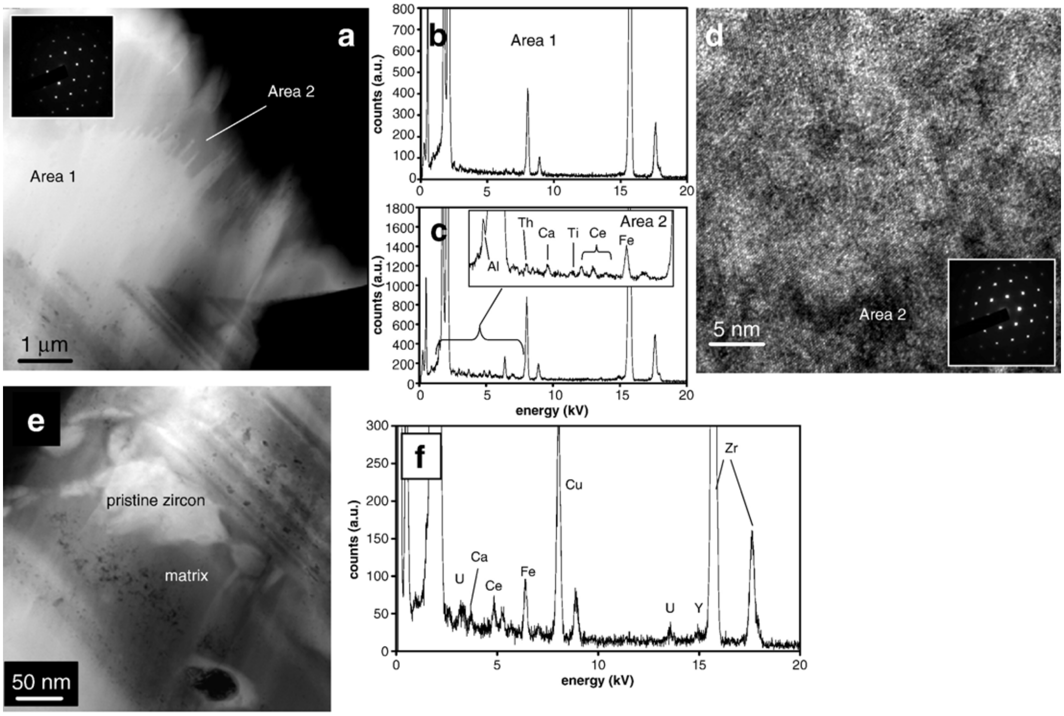

Fig. 9. (a) HAADF-STEM image of the area where zoning is overprinted at spot G in grain T3. Bright and dark zones are labeled area 1 and area 2, respectively. The inset is SAED from area 1. (b) and (c) are EDS from the areas 1 and 2, respectively. The spectrum of area 2 was enlarged in the vertical axis to show the occurrence of trace elements (inset). The Cu-peak is from the Cu-grid. (d) HRTEM image and SEAD (inset) collected from area 2. (e) HAADF-STEM image of the core of grain T3 (spot H). (f) EDS collected from the matrix. The Cu-peak is from the Cu-grid.

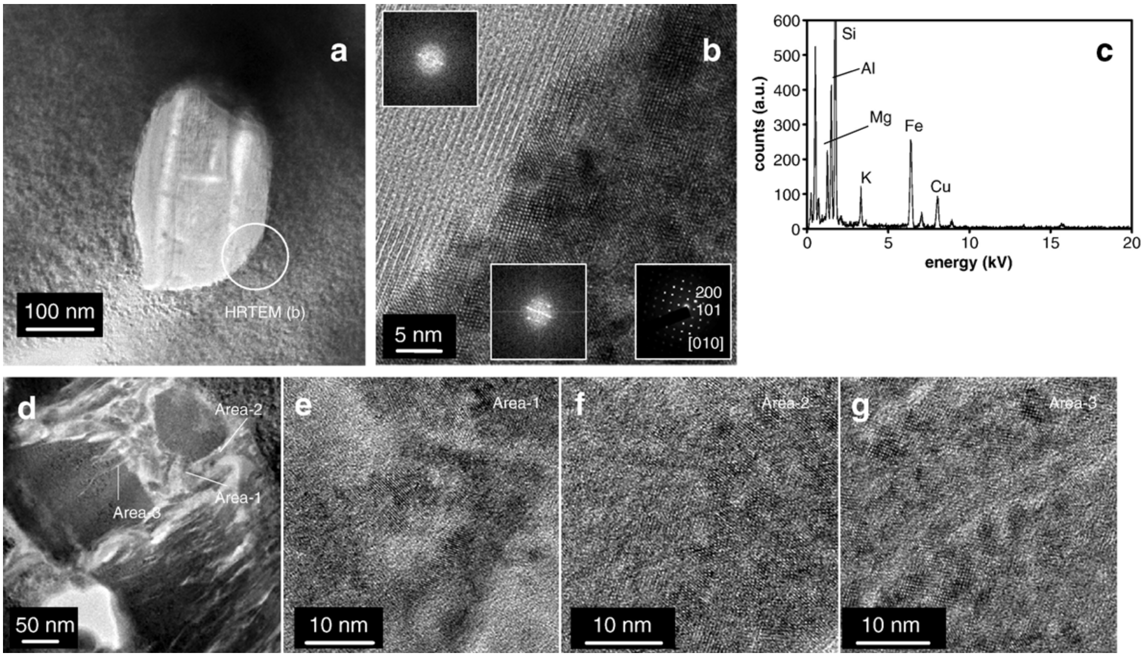

Fig. 10. (a) BFTEM image of a clay inclusion at spot I in grain T4. (b) HRTEM images of the boundary between the clay inclusion and matrix zircon with SAED and FFT pattern (insets). (c) EDS of the clay inclusion. The Cu-peak is from the Cu-grid. (d) BFTEM image of fractured zircon nearby the spot I in grain T4 showing unaltered zircon with clays filling the fracture. HRTEM images (e–g) of area 1 to 3, show highly damaged zircon structures.

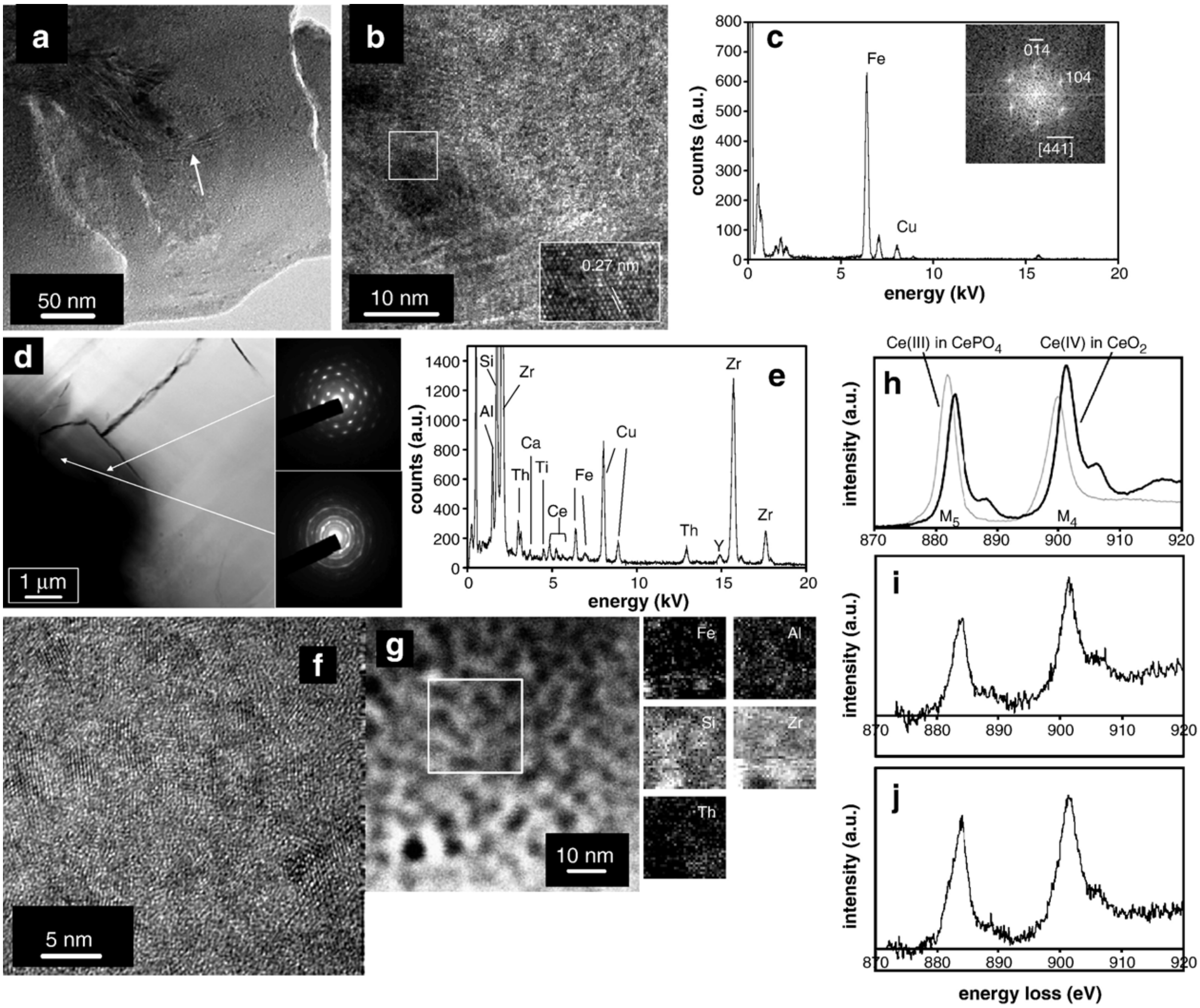

Fig. 11. Spot J in grain T5. (a) BFTEM image of Fe-rich precipitations in damaged zircon. (b) HRTEM image of the Fe-oxide embedded in a highly damaged area. The inset is a magnified image of the Fe-oxide area. (c) The EDS of the Fe-oxide with FFT (inset). The Cu-peak is from the Cu-grid. (d) HAADF-STEM image with SAED patterns from the core of grain T5 (spot K). The ring pattern indicates randomly oriented zircon nanocrystallites. (e) The EDS from the area where the ring SAED pattern was taken. (f) HRTEM image shows that nano-sized zircon crystals are present in an amorphous matrix. (g) HAADF-STEM image and nano-scale elemental maps (Fe, Al, Si, Zr, and Th) corresponding to the region outlined by a square. (h) Background-subtracted EEL spectrum of Ce $M_{4,5}$ edge from two pure minerals; $CePO_4$ and CeO_2, containing Ce(III) and Ce (IV), respectively. (i and j) Two EELS of Ce M-edge from the core of grain T5 (spot K), where randomly oriented zircon nanocrystallites and a large fraction of amorphous domains were observed.

T4, a mixture of broken zircon clusters and clay infilling cracks were observed (Fig. 10d). The fractured zircon remnants are highly damaged with a large amorphous volume as shown in HRTEM (Fig. 10e–g), indicating that physical fractures in zircon tend to occur at highly damaged region.

At spot J in grain T5, precipitation of Fe-oxides was observed (Fig. 11a). The Fe-oxides appear to penetrate into highly damaged zircon (Fig. 11b and c), and, based on the FFT image of a part of HRTEM image, the Fe-oxide was identified as hematite, indicating oxidizing conditions during Fe-precipitation. In addition, the core of this grain, spot K, is extensively altered (Fig. 11d), containing high concentrations of non-formula elements: 2.2 wt.% of Al, 0.21 wt.% of Ca, 2.1 wt.% of Fe, 1.2 wt.% of Y, 0.36 wt.% and 3.7 wt.% of Ce, in the semi-quantitative analysis (Fig. 11e). Possibly, the presence of many fractures, cutting across the zoning, opened pathways for fluids to penetrate into the core of the grain. The altered core consisted of randomly oriented zircon nanocrystallites, based on the ring patterns in SAED and the HRTEM images (Fig. 11d and f). Nano-

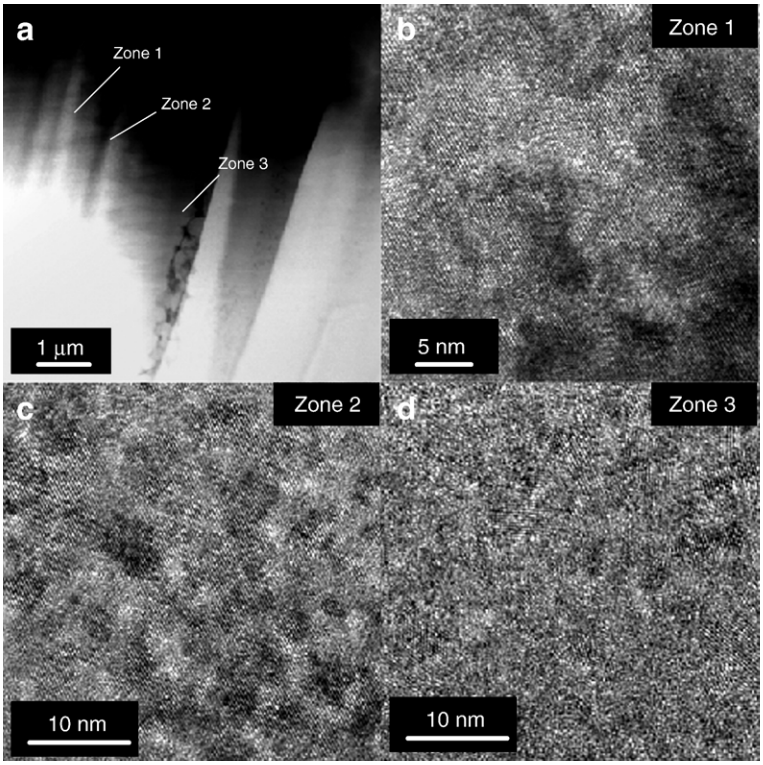

Fig. 12. (a) HAADF-STEM image of zoning and a fracture at spot L in grain T6 (labeled in Fig. 5). (b–d) Series of HRTEM images from zone 1 through 3. Fracture formation and penetration of alteration products preferentially occurs in the highly damaged zone with randomly oriented zircon nanocrystallites (zone 3).

scale elemental mapping was performed to test the distribution of these non-formula elements (Fig. 11g). Although it was extremely difficult to obtain a clear signal due to the limited acquisition time, so as not to destroy the specimen and the low concentration of the non-formula elements, the trace element maps revealed a heterogeneous distribution of Th, Al and Fe in a region of a few tens of nanometers.

An EELS analysis revealed reasonable signal/noise ratio and ELNES (energy-loss near edge shape) for qualitatively determining Ce^{4+}/Ce^{3+} ratio. Two spectra of Ce–M edge were collected from two different points at the core of the grain (spot K) shown in Fig. 11 associated with the EELS profiles of standard end-member Ce-bearing minerals (Fig. 11h); $CePO_4$ and CeO_2 for Ce(III) and Ce(IV), respectively. The two EELS (Fig. 11i and j) have characteristics of Ce^{4+}; that is, the evidence of post-edge small peaks around ~889 and ~906.5 eV, and the ratio of peak height between Ce M_4, and M_5 peaks, as well as the slight chemical shift of these peaks. Based on this qualitative analysis on Ce redox state in this altered region, Ce was determined to be present as Ce^{4+}, suggesting that reducing condition did not occur during the alteration.

Grain T6 showed similar zoning and alteration phases to the other grains as seen in spot L (Fig. 12a): The bright contrast zone consists of crystalline zircon (Fig. 12b and c), while the dark contrast zone consists of randomly oriented zircon nanocrystals (Fig. 12d). The highly damaged dark contrast zone reveals a fracture with precipitation of alteration phases.

4. Discussion

4.1. The percolation point

The concentrations of Ca and Al begin to increase at 0.76 dpa. This marks the beginning of “penetration” of impurities into the zircon structure. Conceptually, this threshold dose, the first percolation point, is the dose at which amorphous domains overlap and become interconnected (Salje et al., 1999); thus, creating a path for the infiltration of impurity elements into the zircon structure. Geisler (2003a) also noted the same phenomenon; however, the concentration of impurity elements began to increase at a dose of 0.95 dpa. Other estimates of threshold dose for the first percolation point are 0.17 dpa (Balan et al., 2001) and 0.07 dpa (Davis and

Krogh, 2000). As Geisler et al. (2003a) has suggested, the different thermal histories of each grain will result in a wide range of threshold doses. Furthermore, the timing of the alteration event is another factor that can cause the threshold dose to vary. The percolation point at a dose of 0.76 dpa is unique for the zircons in the porphyritic granite at Jack Hills. Hoskin (2005) has argued that some zones in the zircons at Jack Hills have reached a high enough level of radiation damage to create interconnected amorphous clusters that allow pathways for the infiltration of hydrothermal fluids after only 125 myr when the cumulative dose reached 1.1×10^{15} (alpha decay events/mg), which is equivalent to 0.05 dpa. The threshold dose of 0.05 dpa is the same percolation point as reported for Sri Lankan zircon by Murakami et al. (1991). However, our results clearly indicate that the dose of the first percolation point in Jack Hills granitoids has a much higher value, ~0.76 dpa, presumably due to thermal annealing.

4.2. Ce anomaly

According to Ballard et al. (2002), the Ce (IV)/Ce (III) ratio in zircon can be calculated based on partitioning between melt and zircon; where:

$$(\mathrm{Ce(IV)}/\mathrm{Ce(III)})_{\mathrm{zircon}} = \frac{\mathrm{Ce}_{\mathrm{melt}} - \frac{\mathrm{Ce}_{\mathrm{zircon}}}{D_{\mathrm{Ce(III)}}^{\mathrm{zircon/melt}}}}{\frac{\mathrm{Ce}_{\mathrm{zircon}}}{D_{\mathrm{Ce(IV)}}^{\mathrm{zircon/melt}}} - \mathrm{Ce}_{\mathrm{melt}}} \qquad (3)$$

$\mathrm{Ce}_{\mathrm{melt}}$ and $\mathrm{Ce}_{\mathrm{zircon}}$ are concentrations of Ce in melt and zircon, respectively, and $D_{\mathrm{Ce(III)}}^{\mathrm{zircon/melt}}$ and $D_{\mathrm{Ce(IV)}}^{\mathrm{zircon/melt}}$ are distribution coefficients of Ce(III) and (IV), respectively. The distribution coefficients calculated by Ballard et al. (2002), based on the lattice-strain model of Blundy and Wood (1994), were used for this calculation. $\mathrm{Ce}_{\mathrm{melt}}$ was assumed to be same as the concentration in the bulk rock of porphyritic granite sample W61, reported by Pidgeon and Wilde (1998). $\mathrm{Ce}_{\mathrm{zircon}}$ was the measured value determined by EMPA. To describe the Ce anomaly as compared with the other REEs, the ratio of chondrite normalized Ce concentration and Ce* was calculated, where Ce* is the average value calculated by the following expression:

$$\mathrm{Ce}^* = ((\mathrm{La}/\mathrm{La}_{\mathrm{CI-chondrite}}) + (\mathrm{Nd}/\mathrm{Nd}_{\mathrm{CI-chondrite}}))/2 \qquad (4)$$

The values of CI-chondrite are from McDonough and Sun (1995). The calculated values of Ce(IV)/Ce(III) are extremely high, >500, and the points analyzed with a higher U-concentration were determined to have even higher values of Ce(IV)/Ce(III), 10^4–10^5. In this study, variations in the Ce(IV)/Ce(III) ratio at such high levels (>500) does not reflect the actual redox state except for the data from unaltered zones, because a considerable amount of Ce was apparently introduced during the intensive alteration. However, we have inferred that the redox state of Ce in the unaltered portion of zircons is dominated by Ce(IV). This is consistent with the direct determination of the oxidation state by EELS, which reveals mainly tetravalent Ce (Fig. 11h–j).

Compared with the Ce-concentrations in typical zircons (e.g., 3–160 ppm (Hoskin and Schaltegger, 2003)), the Ce-concentration in the altered zone of the present suite of zircons (dark contrast zones both in BSE image and HAADF-STEM image) is extremely high, 1–2 wt.% (Table 1). Semi-quantitative EDS analysis in the altered zone gave even higher concentrations, such as at spot K (Fig. 11e), 3.7 wt.% of Ce. However, even in the areas with high Ce-concentrations, Ce-bearing inclusions such as monazite were not observed. Thus, almost all of Ce present in the altered zircon is a result of alteration by fluids with a range of Ce/Al ratios.

The Ce-anomaly index, Ce/Ce* is plotted as a function of the calculated dose and the Al-concentration (Fig. 13). The Ce/Ce* index varies from 1 to 6 for each grain, but the values for each grain are almost constant as both the calculated dose increases and alteration progresses. Hoskin and Schaltegger (2003) have also reported a Ce-anomaly and high concentrations of LREE in the Jack Hills zircon. Our data, plotted as a function of the alpha-decay dose, suggest that the LREE pattern is overprinted by a later alteration event and that the addition of the REE pattern of alteration fluids did not modify the LREE pattern significantly.

The timing of the alteration that delivered REEs is not certain, but the previous isotopic study of zircons from this locality has reported the possibility of low temperature alteration 200 my ago (Pidgeon and Wilde, 1998). The oxidized form of Ce (tetravalent) in altering fluids is consistent with the oxidizing environment at the Earth's surface at the time of the alteration. The timing of thermal events is difficult to estimate because the annealing effect is a combined function of time and temperature.

4.3. Nano-structure of zircon

Based on the TEM results: (i) a number of pores were observed at the various sizes, up to ~100 nm, within almost all grains. The presence of many pores at the nano-scale has been considered as a factor in facilitating chemical transport to and from the reaction front, and the pores probably formed by volume reduction during

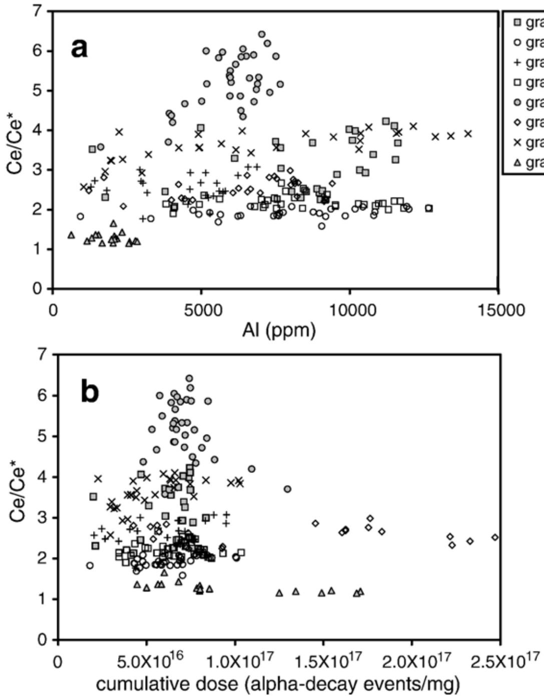

Fig. 13. (a) Ce-anomaly index, Ce/Ce* vs. Al (ppm). (b) Ce/Ce* vs. the calculated dose. Each symbol corresponds to the data from an individual grain.

the amorphous-to-crystalline transition (Geisler et al., 2004) during annealing. These pores are surrounded by crystalline zircon, indicating that zones containing pores have recrystallized; (ii) zones with high U-concentrations contain relatively high concentrations of non-formula elements (Fig. 11), including Al and Ca. Randomly oriented zircon nanocrystals are present in the highly-damaged portion that has a high U-content, up to 1 wt.%. Most likely, the non-formula elements are present within the amorphous domains; (iii) Fe occurs as various forms: oxide inclusions in originally zoned zircon and as hematite precipitates in radiation damaged zones, and trace amounts in phengite clays; (iv) clay minerals, possibly phengite, occur as inclusions and infilling fractures; (v) fully amorphized zircons were not observed; (vi) fractures occur preferentially in the more highly damaged zones.

The fact that fully metamict domains were not observed in any of the zircon grains, despite the calculated high radiation dose, is strong evidence for thermal annealing. Zircons from outcropping granite at another locality in the Jack Hills (W31) were previously studied using Raman spectroscopy to evaluate radiation damage accumulation (Nasdala et al., 2001). They concluded that this locality had experienced a “hot” annealing event in the Proterozoic (~980 Ma), which is consistent with the fact that U–Pb discordia intercepted concordia at 2659 and 980 Ma, as determined by SIMS (Pidgeon, 1992). However, the temperature of the “hot” annealing event was not determined.

According to Meldrum et al. (1998a) and Meldrum et al. (1998b), radiation damage at temperatures higher than ~740 °C produces decomposition of zircon into ZrO_2 and amorphous silica. TEM study of the Jack Hills zircons did not reveal any evidence of ZrO_2 in the damaged zones, suggesting that the annealing temperature was never higher than ~740 °C. In addition, an annealing study of metamict zircon probed by HRTEM reported that recrystallization started at 730–930 °C, forming randomly oriented ZrO_2 in amorphous silica; and at higher temperature, 1330 °C (highly metamict) and 1130 °C (partially metamict), randomly oriented zircon nano-grains recrystallized with the grain boundary forming polygonal texture (Capitani et al., 2000). This is in contrast to the results of an EXAFS study that reported structural recovery at 900 °C (Farges, 1994). Although the recrystallized zircon grains with the polygonal boundaries (Capitani et al., 2000) are randomly oriented, the grain size and the occurrence are different from the zircon nanocrystals found in the present study. Zircon crystallites with polygonal boundaries are larger (a few hundred nm) due to annealing and lack of amorphous domains around the zircon crystallites. Thus, the W61 zircons were not recrystallized at high temperature, and by inference, the annealing temperature was less than 730 °C.

In terms of the process of formation of the randomly oriented nanocrystals of zircon, early HRTEM studies on natural zircons from Sri Lanka proposed a damage accumulation process (Murakami et al., 1991). The zircon structure is gradually and heterogeneously dominated by the overlap of nano-scale-sized amorphous domains with crystalline remnants “floating” in an amorphous matrix. The crystallites rotate to form low angle grain boundaries in the highly damaged state (stage II). At no stage of the damage were the crystallites randomly oriented, rather they form low angle grain boundaries with one another (Murakami et al., 1991). McLaren et al. (1994) and Palenik et al. (2003) also examined damaged zircons from Sri Lanka using HRTEM and noted diffused spots in diffraction patterns, but they did not report any ring pattern in the SAED of the randomly oriented nanocrystals of zircon. In addition, heavy-ion irradiation studies of zircon have shown that zircon nanocrystallites, within the amorphous matrix, were rotated to form low-angle grain boundaries during the crystalline-to-amorphous transition, but no randomly oriented nanocrystallites of zircon were observed (Wang et al., 1993; Wang, 1998).

Hydrothermal experiments on a Sri Lanka zircon at 450 °C showed that local recrystallization is catalyzed by the presence of altering solutions, leading to a decreased Th/U ratio (Geisler et al., 2001). A subsequent systematic study by Geisler et al. (2003b) proposed that the hydrothermal alteration of zircon does not occur by a process of simple dissolution and reprecipitation, but rather, the process is a sequence of steps that involve water diffusion, reaction, and recrystallization. They developed a volume diffusion model of this process (Geisler et al., 2002). A subsequent experiment showed that the limited loss or gain of U, Th and REE was observed in the high temperature fluids (at ~650 °C). In contrast, the experiment with low temperature fluids (350 and 175 °C) showed a significant loss of trace elements (Geisler et al., 2003b). For the zircon from Jack Hills, a large quantity of the non-formula elements; Al, Ca, Fe and REE, were introduced during alteration, which suggests that the temperature of the alteration was not higher than 650 °C.

5. Conclusions

Based on our observations of nano-scale structural and compositional variations in these 3.3 Ga zircons, a number of important insights were obtained:

(i) A variety of secondary alteration phases were identified. Phengite was present in the fractures and pores at the size range from a few ten nanometers to a few microns in the zircon. Hematite and other Fe-oxide phases were found in the radiation-damaged areas and in some pores. These inclusions often occur in the recrystallized zones. Thus, careful attention to the presence of inclusions is required in order to avoid these impurity phases during ion probe analysis.

(ii) Cumulative radiation doses in these zircons reach values up to 1.5×10^{17} alpha-decay events/mg (=7.3 dpa). These radiation doses are much higher than what is required for complete amorphization, as determined by Murakami et al. (1991) and an ion irradiation experiment (Meldrum et al., 1998a). Remarkably, fully-amorphous domains were absent in these ancient zircons. This must be due to simultaneous thermal annealing during damage-accumulation, and this explains the high structural stability of the zircons from this locality over the past 3.3 Ga.

(iii) The first percolation point occurs at an alpha-decay event dose of 0.76 dpa. Even though this percolation point was determined for the zircons from Jack Hills, this value cannot be directly applied to the zircon in the adjacent metasedimentary rocks, because the source rock and the age of zircons from the metasedimentary rock are different from the zircons in the porphyritic granite of the present study. This high dose for the first percolation point is evidence of extensive annealing. This may explain the high chemical durability of these zircons and their ability to retain ancient isotopic signatures. Once the radiation dose exceeds the first percolation point, alteration is evidenced by the large amounts of impurity elements (Ca, Al, Fe and rare earth elements) that are found in the amorphous domains. However, U and Th are still retained in the amorphous domains. This is noteworthy in considering the use of zircon as a nuclear waste form for actinides.

Acknowledgements

The authors are grateful to the staff at the Electron Microbeam Analysis Laboratory (EMAL) of University of Michigan. The authors are also indebted to Drs. T. Geisler, P.W.O. Hoskin, and D. Cherniak for their helpful review comments that greatly improved this paper. We also thank the editor, Dr. C. Göpel, for his valuable comments and handling the manuscript with patience. This work was supported by National Science Foundation (NIRT), EAR-0403732 and Office of Basic Energy Sciences, U.S. Department of Energy (DEFG02ER45656).

References

Aines, R.D., Rossman, G.R., 1986. Relationship between radiation damage and trace water in zircon, quartz and topaz. Am. Mineral. 71, 1186–1193.

Balan, E., Neuville, D.R., Trocellier, P., Fritsch, E., Muller, J.P., Calas, G., 2001. Metamictization and chemical durability of detrital zircon. Am. Mineral. 86, 1025–1033.

Ballard, J.R., Palin, J.M., Campbell, I.H., 2002. Relative oxidation states of magmas inferred from Ce(IV)/Ce(III) in zircon: application to porphyry copper deposit of northern Chile. Contrib. Mineral. Petrol. 144, 347–364.

Blundy, J., Wood, B., 1994. Prediction of crystal-melt partition coefficients from elastic moduli. Nature 372, 452–454.

Breeding, C.M., Ague, J.J., Grove, M., Rupke, A.L., 2004. Isotopic and chemical alteration of zircon by metamorphic fluids: U–Pb age depth-profiling of zircon crystals from Barrow's garnet zone, northeast Scotland. Am. Mineral. 89, 1067–1077.

Capitani, G.C., Leroux, H., Doukhan, J.C., Rios, S., Zhang, M., Salje, E.K.H., 2000. A TEM investigation of natural metamict zircons: structure and recovery of amorphous domains. Phys. Chem. Miner. 27, 545–556.

Cavosie, A.J., Wilde, S.A., Liu, D., Weiblen, P.W., Valley, J.W., 2004. Internal zoning and U–Th–Pb chemistry of Jack Hills detrital zircons: a mineral record of early Archean to Mesoproterozoic (4348–1576 Ma) magmatism. Precambrian Res. 135, 251–279.

Cavosie, A.J., Wilde, S.A., Valley, J.W., E.I.M.F., 2005. Magmatic δ^{18}O in 4400–3900 Ma detrital zircons: a record of the alteration and recycling of crust in the Early Archean. Earth Planet. Sci. Lett. 235, 663–681.

Cherniak, D.J., Watson, B.W., 2000. Pb diffusion in zircon. Chem. Geol. 172, 5–24.

Cherniak, D.J., Lanford, W.A., Ryerson, F.J., 1991. Lead diffusion in apatite and zircon using ion implantation and Rutherford backscattering techniques. Geochim. Cosmochim. Acta 55, 1663–1673.

Compston, W., Pidgeon, R.T., 1986. Jack Hills, evidence of more very old detrital zircons in Western Australia. Nature 321, 766–769.

Compston, W., Froude, D.O., Ireland, T.R., Kinny, P.D., Williams, I.S., Williams, I.R., Myers, J.S., 1985. The age of (a tiny part of) the Australian continent. Nature 317, 559–560.

Craig, H., 1968. Zircon lead loss — a kinetic model. Science 159, 447.

Davis, D.W., Krogh, T.E., 2000. Preferential dissolution of 234U and radiogenic Pb from α-recoil-damaged lattice sites in zircon: implications for thermal histories and Pb isotopic fractionation in the near surface environment. Chem. Geol. 172, 41–58.

Davis, D.W., Williams, I.S., Krogh, T.E., 2003. Historical development of zircon geochronology. In: Hanchar, J.M., Hoskin, P.W.O. (Eds.), Reviews in Mineralogy and Geochemistry. Mineral. Soc. Am., vol. 53, pp. 145–181.

Drake, M.J., Weill, D.F., 1972. New rare earth elements standards for electron microprobe analysis. Chem. Geol. 10, 179–181.

Ewing, R.C., 1999. Nuclear waste forms for actinides. Proc. Natl. Acad. Sci. U. S. A. 96, 3432–3439.

Ewing, R.C., 2005. Plutonium and "minor" actinides: safe sequestration. Earth Planet. Sci. Lett. 229, 165–181.

Ewing, R.C., Haaker, R.F., Lutze, W., 1982. Leachability of zircon as a function of alpha dose. Proceedings of Material Research Society Symposium, vol. 11, pp. 389–397.

Ewing, R.C., Chakoumakos, B.C., Lumpkin, G.R., Murakami, T., Greegor, R.B., Lytle, F.W., 1988. Metamict minerals: natural analogues for radiation damage effects in ceramic nuclear waste forms. Nucl. Instrum. Methods Phys. Res., B Beam Interact. Mater. Atoms 32, 487–497.

Ewing, R.C., Lutze, W., Weber, W.J., 1995. Zircon: a host-phase for the disposal of weapons plutonium. J. Mater. Res. 10, 243–246.

Ewing, R.C., Meldrum, A., Wang, L.M., Wang, S.X., 2000. Radiation-induced amorphization. In: Redfern, S.A.T., Carpenter, M.A. (Eds.), Transformation Processes in Minerals: Reviews in Mineralogy and Geochemistry. Mineralogical Society of America, vol. 39, pp. 319–361.

Ewing, R.C., Meldrum, A., Wang, L., Weber, W.J., Corrales, L.R., 2003. Radiation effects in zircon. In: Hanchar, J.M., Hoskin, P.W.O. (Eds.), Reviews in Mineralogy and Geochemistry. Mineral. Soc. Am., vol. 53, pp. 387–425.

Farges, F., 1994. The structure of metamict zircon: a temperature-dependent EXAFS study. Phys. Chem. Miner. 20, 504–514.

Froude, D.O., Ireland, T.R., Kinny, P.D., Williams, I.S., Compston, W., Williams, I.R., Myers, J.S., 1983. Ion microprobe identification of 4,100–4,200 Myr-old terrestrial zircons. Nature 304, 616–618.

Garvie, L.A.J., Buseck, P.R., 1999. Determination of Ce^{4+}/Ce^{3+} in electron-beam-damaged CeO_2 by electron energy-loss spectroscopy. J. Phys. Chem. Solids 60, 1943–1947.

Geisler, T., Schleicher, H., 2000. Improved U–Th-total Pb dating of zircons by electron microprobe using a simple new background modeling procedure and Ca as a chemical criterion of fluid-induced U–Th–Pb discordance in zircon. Chem. Geol. 163, 269–285.

Geisler, T., Ulonska, M., Schleicher, H., Pidgeon, R.T., van Bronswijk, W., 2001. Leaching and differential recrystallization of metamict zircon under experimental hydrothermal conditions. Contrib. Mineral. Petrol. 141, 53–65.

Geisler, T., Pidgeon, R.T., van Bronswijk, W., Kurtz, R., 2002. Transport of uranium, thorium, and lead in metamict zircon under low-temperature hydrothermal conditions. Chem. Geol. 191, 141–154.

Geisler, T., Rashwan, A.A., Rahn, M.K.W., Poller, U., Zwingmann, H., Pidgeon, R.T., Schleicher, H., Tomaschek, F., 2003a. Low-temperature hydrothermal alteration of natural metamict zircons from the Eastern Desert, Egypt. Mineral. Mag. 67, 485–508.

Geisler, T., Pidgeon, R.T., Kurtz, R., van Bronswijk, W., Schleicher, H., 2003b. Experimental hydrothermal alteration of partially metamict zircon. Am. Mineral. 88, 1496–1513.

Geisler, T., Zang, M., Salje, E.K.H., 2003c. Recrystallization of almost fully amorphous zircon under hydrothermal conditions: an infrared spectroscopic study. J. Nucl. Mater. 320, 280–291.

Geisler, T., Seydoux-Guillaume, A., Wiedenbeck, M., Wirth, R., Berndt, J., Zhang, M., Mihailova, B., Putnis, A., Salje, E.K.H., Schlüter, J., 2004. Periodic precipitation pattern formation in hydrothermally treated metamict zircon. Am. Miner. 89, 1341–1347.

Hanchar, J.M., Finch, R.J., Hoskin, P.W.O., Watson, E.B., Cherniak, D.J., Mariano, A.N., 2001. Rare earth elements in synthetic zircon: Part 1. Synthesis, and rare earth element and phosphorus doping. Am. Miner. 86, 667–680.

Hoskin, P.W.O., 2005. Trace-element composition of hydrothermal zircon and the alteration of Hadean zircon from the Jack Hills, Australia. Geochim. Cosmochim. Acta 69, 637–648.

Hoskin, P.W.O., Schaltegger, U., 2003. The composition of zircon and igneous and metamorphic petrogenesis. In: Hanchar, J.M., Hoskin, P.W.O. (Eds.), Reviews in Mineralogy and Geochemistry. Mineral. Soc. Am., vol. 53, pp. 27–62.

Krogh, T.E., 1973. A low-contamination method for hydrothermal decomposition of zircon and extraction of U and Pb for isotopic age determinations. Geochim. Cosmochim. Acta 37, 485–494.

Krogh, T.E., Davis, G.L., 1975. Alteration in zircons and differential dissolution of altered and metamict zircon. Carnegie Inst. Washington, Year Book 74, 619–623.

Maas, R., McCulloch, M.T., 1991. The province of Archean clastic metasediments in the Narryer gneiss complex, western Australia: trace element geochemistry, Nd isotopes, and U–Pb ages for detrital zircons. Geochim. Cosmochim. Acta 55, 1915–1932.

Maas, R., Kinny, P.D., Williams, I.S., Froude, D.O., Compston, W., 1992. The Earth's oldest known crust: a geochronological and geochemical study of 3900–4200 Ma old detrital zircons from Mt. Narryer and Jack Hills, western Australia. Geochim. Cosmochim. Acta 56, 1281–1300.

McDonough, W.F., Sun, S.-s S., 1995. The composition of the Earth. Chem. Geol. 120, 223–253.

McLaren, A.C., Fitz Gerald, J.D., Williams, I.S., 1994. The microstructure of zircon and its influence on the age determination from Pb/U isotopic ratios measured by ion microprobe. Geochim. Cosmochim. Acta 58, 993–1005.

Meldrum, A., Zinkle, S.J., Boatner, L.A., Ewing, R.C., 1998a. A transient liquid-like phase in the displacement cascades of zircon, hafnon and thorite. Nature 395, 56–58.

Meldrum, A., Boatner, L.A., Weber, W.J., Ewing, R.C., 1998b. Radiation damage in zircon and monazite. Geochim. Cosmochim. Acta 62, 2509–2520.

Mojzsis, S.J., Harrison, T.M., Pidgeon, R.T., 2001. Oxygen-isotope evidence from ancient zircons for liquid water at the Earth's surface 4300 Myr ago. Nature 409, 178–181.

Murakami, T., Chakoumakos, B.C., Lumpkin, G.R., Weber, W.J., 1991. Alpha-decay event damage in zircon. Am. Mineral. 76, 1510–1532.

Myers, J.S., 1988. Early Archean Narryer gneiss complex, Yilgarn craton, western Australia. Precambrian Res. 38, 297–307.

Myers, J.S., Williams, I.R., 1985. Early Precambrian crustal evolution at Mount Narryer, western Australia. Precambrian Res. 27, 153–163.

Nasdala, L., Wenzel, M., Vavra, G., Irmer, G., Wenzel, T., Kober, B., 2001. Metamictisation of natural zircon: accumulation versus thermal annealing of radioactivity-induced damage. Contrib. Mineral. Petrol. 141, 125–144.

Nasdala, L., Reiners, P.W., Garver, J.I., Kennedy, A.K., Stern, R.A., Balan, E., Wirth, R., 2004. Incomplete retention of radiation damage in zircon from Sri Lanka. Am. Mineral. 89, 219–231.

Nelson, D.R., Robinson, B.W., Myers, J.S., 2000. Complex geological histories extending for ≥ 4.0 Ga deciphered from xenocryst zircon microstructures. Earth Planet. Sci. Lett. 181, 89–102.

Nutman, A.P., Kinny, P.D., Compston, W., Williams, I.S., 1991. SHRIMP U–Pb zircon geochronology of the Narryer gneiss complex, western Australia. Precambrian Res. 52, 275–300.

Palenik, C.S., Nasdala, L., Ewing, R.C., 2003. Radiation damage in zircon. Am. Mineral. 88, 770–781.

Peck, W.H., Valley, J.W., Wilde, S.A., Graham, C.M., 2001. Oxygen isotope ratios and rare earth elements in 3.3 to 4.4 Ga zircons: ion microprobe evidence for high s 18O continental crust and ocean in the Early Archean. Geochim. Cosmochim. Acta 65, 4215–4229.

Pennycook, S.J., Jesson, D.E., 1990. High-resolution incoherent imaging of crystals. Phys. Rev. Lett. 64, 938–941.

Pidgeon, R.T., 1992. Recrystallization of oscillatory zoned zircon: some geochronological and petrological implications. Contrib. Mineral. Petrol. 110, 463–472.

Pidgeon, R.T., Wilde, S.A., 1998. The interpretation of complex zircon U–Pb systems in Archaean granitoids and gneisses from the Jack Hills, Narryer Gneiss Terrane, Western Australia. Precambrian Res. 91, 309–332.

Pidgeon, R.T., O'Neil, J.R., Silver, R.T., 1966. Uranium and lead isotopic stability in a metamict zircon under experimental hydrothermal conditions. Science 154, 1538–1540.

Ríos, S., Salje, E.K.H., Zhang, M., Ewing, R.C., 2000. Amorphization in zircon: evidence for direct impact damage. J. Phys. Condens. Matter 12, 2401–2412.

Rizvanova, N.G., Levchenkov, O.A., Belous, A.E., Bezmen, N.I., Maslenikov, A.V., Komarov, A.N., Makeev, A.F., Levskiy, L.K., 2000. Zircon reaction and stability of the U–Pb isotope system during interaction with carbonate fluid: experimental hydrothermal study. Contrib. Mineral. Petrol. 139, 101–114.

Salje, E.K.H., Chrosch, J., Ewing, R.C., 1999. Is "metamictization" of zircon a phase transition? Am. Mineral. 84, 1107–1116.

Sinha, A.K., Wayne, D.M., Hewitt, D.A., 1992. The hydrothermal stability of zircon: preliminary experimental and isotopic studies. Geochim. Cosmochim. Acta 56, 3535–3551.

Utsunomiya, S., Ewing, R.C., 2003. Application of high-angle annular dark field scanning transmission electron microscopy, scanning transmission microscopy-energy dispersive X-ray spectrometry, and energy-filtered transmission electron microscopy to the characterization of nanoparticles in the environment. Environ. Sci. Technol. 37, 786–791.

Utsunomiya, S., Palenik, C.S., Valley, J.W., Cavosie, A.J., Wilde, S.A., Ewing, R.C., 2004. Nanoscale occurrence of Pb in an Archean zircon. Geochim. Cosmochim. Acta 68, 4679–4686.

Utsunomiya, S., Yudintsev, S., Ewing, R.C., 2005. Radiation effects in ferrate garnet. J. Nucl. Mater. 336, 251–260.

Valley, J.W., 2003. Oxygen isotopes in zircon. In: Hanchar, J.M., Hoskin, P.W.O. (Eds.), Reviews in Mineralogy and Geochemistry. Mineral. Soc. Am., vol. 53, pp. 343–385.

Valley, J.W., Chiarenzelli, J.R., McLelland, J.M., 1994. Oxygen isotope geochemistry of zircon. Earth Planet. Sci. Lett. 126, 187–206.

Valley, J.W., Peck, W.H., King, E.M., Wilde, S.A., 2002. A cool early Earth. Geology 30, 351–354.

Wang, L.M., 1998. Applications of advanced electron microscopy techniques to the studies of radiation effects in ceramic materials. Nucl. Instrum. Methods Phys. Res., B Beam Interact. Mater. Atoms 141, 312–325.

Wang, L.M., Ewing, R.C., Weber, W.J., 1993. Temperature and ion-mass dependence of amorphization dose for ion beam irradiated zircon ($ZrSiO_4$). Mater. Res. Soc. Symp. Proc. 279, 451–456.

Watson, E.B., Harrison, T.M., 2005. Zircon thermometer reveals minimum melting conditions on earliest Earth. Science 308, 841–844.

Weber, W.J., 1991. Self-radiation damage and recovery in Pu-doped zircon. Rad. Eff. Def. Solid 115, 341–349.

Weber, W.J., 2002. Radiation effects in crystalline oxide host phases for the immobilization of actinides. Mater. Res. Soc. Symp. Proc. 713, 443–454.

Weber, W.J., Ewing, R.C., Wang, L.M., 1994. The radiation-induced crystalline-to-amorphous transition in zircon. J. Mater. Res. 9, 688–698.

Weber, W.J., Ewing, R.C., Meldrum, A., 1997. The kinetics of alpha-decay-induced amorphization in zircon and apatite containing weapons-grade plutonium or other actinides. J. Nucl. Mater. 250, 147–155.

Weber, W.J., Ewing, R.C., Catlow, C.R.A., de la Rubia, T.D., Hobbs, L.W., Kinoshita, C., Matzke, H., Motta, A.T., Nastasi, M., Salje, E.K.H., Vance, E.R., Zinkle, S.J., 1998. Radiation effects in crystalline ceramics for the immobilization of high-level nuclear waste and plutonium. J. Mater. Res. 13, 1434–1484.

Wilde, S.A., Valley, J.W., Peck, W.H., Graham, C.M., 2001. Evidence from detrital zircons for the existence of continental crust and oceans on the Earth 4.4 Gyr ago. Nature 409, 175–178.

Ziegler, J.F., Biersack, J.P., Littmark, U., 1985. The Stopping and Range of Ions in Solids. Pergamon Press, New York.